

The direct numerical simulation of two-phase flows with interface capturing methods

La simulation numérique directe des écoulements diphasiques avec les méthodes de capture d'interface

Sanjoy Banerjee*

banerjee@engineering.ucsb.edu

Vittorio Badalassi

badalass@engineering.ucsb.edu

Vinay Dwivedi

vinay@engineering.ucsb.edu

Jean-Christophe Nave

jcnave2@hotmail.com

David Hall

halldm@physics.ucsb.edu

University of California, Santa Barbara, CA 93106

*Phone: -1-805-893-3456, Fax: +01 805-893-4731

Les écoulements polyphasiques jouent un rôle central dans les problèmes liés à l'environnement et à l'industrie. Les traits communs, mais significatifs, de tels problèmes sont des géométries et une topographie complexes, des processus de transfert à travers des frontières de phase, et des interfaces internes qui fusionnent, déferlent, et se déforment. Les conditions pour prévoir le mouvement des liquides dans de telles conditions représentent des défis importants pour la dynamique des fluides numérique, en particulier pour la simulation directe des écoulements impliquant des interfaces internes. Dans cet article, nous nous concentrerons sur deux modèles qui capturent le mouvement des interfaces internes implicitement et peuvent résoudre des écoulements complexes jusqu'à la taille de la grille informatique. Les méthodes sont basées sur l'approche des champs de phase — qui sont également appliquées dans la forme générale à des systèmes polymères viscoélastiques et avec séparation de phase — dans ce dernier cas en utilisant une approche théorique de champ auto-consistant. Pour des processus de très petites échelles de longueur, e.g. nucléation et croissance, de tels calculs conduisent à des interfaces d'épaisseur finies et avec la physique adéquate. Pour les structures polyphasiques de plus grande dimension-, l'interface devient une discontinuité de contact, et la méthode tend doucement vers une formulation semblable à des ensembles des niveaux. Cependant, dans cette deuxième forme l'interface raide est difficile à traiter par le calcul. Une variation de la méthode du fluide fantôme dans laquelle des interfaces raides peuvent être capturées sera présentée. Des applications seront données aux deux extrémités des échelles, incluant les premiers stades de nucléation, de croissance et de mélange de structures polyphasiques, aussi bien que des écoulements macroscopiques dans lesquels les échelles de longueur et les vitesses sont grands.

I ■ INTRODUCTION

With the advent of increasingly powerful computers, the direct simulation of multiphase flows has become possible. The work is still limited to laminar systems, as simultaneous resolution of turbulence is still too onerous for existing capabilities. Nonetheless, much has been learned about multiphase systems, particularly those at micro- or sub-micro scales, where fluid turbulence is not a problem. In direct simulations, all scales of motion and all interfacial configurations are resolved. This is possible in a variety of simple problems, from which physical insight as to the interfacial transport processes can be derived. For larger-scale applications, a form of super-grid resolution of interfaces may be attempted, and the procedure is sketched in *figure 1*. Here, the subgrid scales, which may involve small bubbles or drops, are treated by something like the multifield model discussed in Part I. However, supergrid scales are fully resolved. This approach is somewhere in between direct simulations and the interpenetrating continua approach, as models and closure relationships are only necessary for the finely-dispersed phases of sub-grid scale, which can often be treated with homogeneous equilibrium or other simple approximations.

In this paper, we will not discuss this approach further here. Suffice it to say that it has great promise for application to practical problems, as it is the closure relationships for the large-scale structures that are most difficult to obtain in the framework of the multifield model (interpenetrating continua model).

To proceed, several methods are available for resolving interfaces directly and satisfying all boundary conditions at them for multiphase systems. These are: VOF, Direct Interface Tracking, Level Sets, and Phase Field.

We will concentrate here on the level-set, also in a form that captures sharp interfaces, and phase-field methods. In addition, we will also discuss, in brief, generalizations of the phase-field method, which allow complex fluid formulations to be treated, such as within the framework of two-fluid and self-consistent field theoretic models. The two-fluid model allows treatment of viscoelastic fluids that are important in a variety of situations, and the model and its applications will be described, as will the field theoretic approach. The last is important in computations of self-assembling multiphase systems, which are of great interest in many industrial applications.

To take an example, consider *figure 2*, which shows a self-assembled polymer template made by IBM, where the structures are of 10 nm in diameter. Such structures are much smaller than the wavelength of light, which is currently used to etch tiny subcircuitry on chips. However, such self-assembled structures can act as part of devices that form a type of flash memory, which in turn retains recent



Figure 1: Schematic of computational grid with a supergrid structure, shown as a slug, and subgrid structures, shown as drops or bubbles.

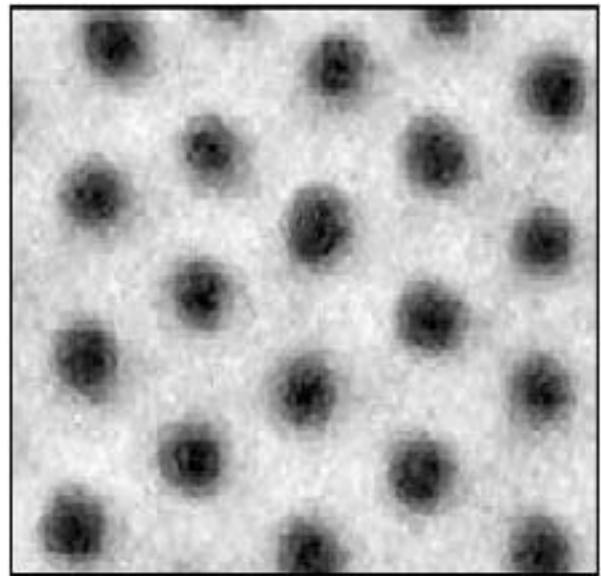


Figure 2: A template proposed by IBM for nanolithography of flash memories. The template is made from a self-assembled polymeric system.

information when an electronic gadget is turned off. IBM notes that such self-assembled structures can also be used to do nanoscale lithography on specially prepared wafers. In any case, self-consistent field-theoretic methods can be used to predict such multiphase structures, which may take the form of cylinders, lamellae, gyroids, and the like, depending on various processing conditions.

Other applications of such direct simulation techniques are for complex fluid product formulation, such as cosmetics, paints, polymeric alloys, and a variety of pharmaceutical and personal care products. Such computational approaches can be used to rapidly screen product formulations and reduce the time taken in trial-and-error experimentation that currently is used. *Figure 3* shows a variety of typical products in which property is affected by the micro/nano structures and where computer models may prove useful in exploring the parameter space, leading to marketable formulations and prediction of physical properties. These fluids are complex in the sense that they are heterogeneous, have multiple phases and, often, non-Newtonian rheology.

Of course, there are more process-oriented applications of such direct simulation technology in equipment, such as condensers, evaporators, crystalizers, bubble columns, and the like. However, since many of these operate at fairly high Reynolds numbers, the simulations have to accommodate some form of turbulence model at the present time. With regard to the various techniques for direct simulation available, reference should be made to the papers by Lauffaurie *et al.*, 1994 (for early treatment of the volume of fluid (VOF) method), Unverdi and Tryggvason, 1992 (for interface tracking), and to Osher and Sethian 1988, Sussman *et al.* 1994, Beux and Banerjee (1997), and Takahira *et al.* 2004 (for level-set methods). For phase-field methods, an excellent review of the model is available in Bray 1994, and simulation methodology in Badalassi *et al.* 2003. As mentioned earlier, the focus in this paper will be on the last two methods. To proceed, we will initiate the discussion by considering level sets.

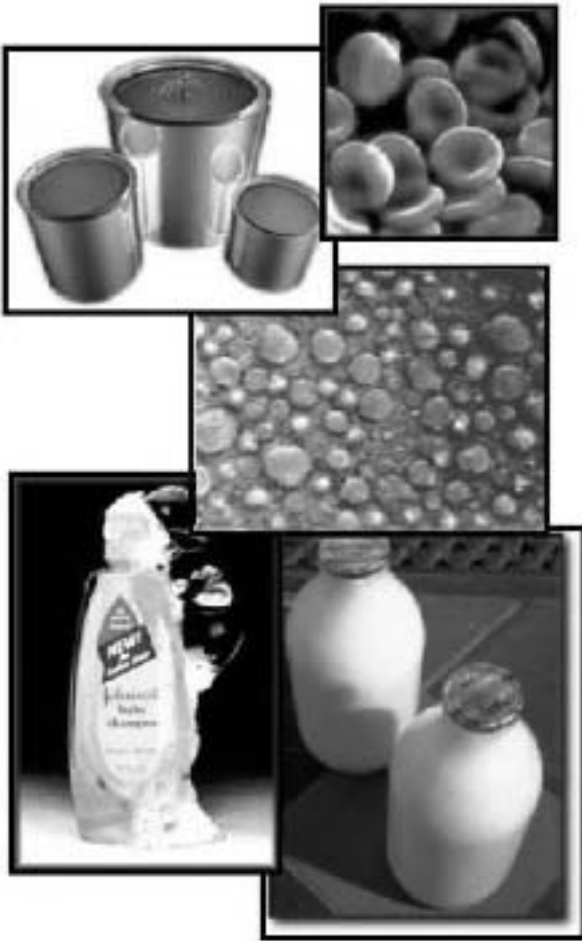


Figure 3: Typical products involving complex fluids.

II ■ THE LEVEL-SET METHOD

The essence of the method is the solution of the following field-equation for the level-set function, ϕ , which has the sense of a distance function (Sethian and Osher (1988)), from the interface at $\phi = 0$.

$$\frac{\partial \phi}{\partial t} + \vec{u} \cdot \nabla \phi = S \tag{1}$$

where

$S = 0$ if there is mean transfer due to phase change across the interfaces

$S = \dot{m} \|\nabla \phi\|$ where \dot{m} is the mass flux of a phase at the interface divided by its density.

The density and molecular viscosity (or turbulent viscosity) are then

$$\rho(\phi) = 1 + (1 - \lambda)H(\phi) \tag{2}$$

$$\eta(\phi) = \eta + (1 - \eta)H(\phi) \tag{3}$$

where $\lambda = \rho_g / \rho_l$ and $\eta = \eta_g / \eta_l$. The Heaviside function, H , may be written in many ways, in a form that we will briefly discuss later even as a discontinuous function. For the present we will use,

$$H(\phi) = \begin{cases} 0 & \text{if } -\phi < -\epsilon \\ 1/2\{1 + \phi/\epsilon + (1/\pi) \sin(\pi\phi/\epsilon)\} & \text{if } -\epsilon < \phi < \epsilon \\ 1 & \text{if } \phi > \epsilon \end{cases} \tag{4}$$

ϵ is a thickness of the interface and is some constant, β , into the spatial discretization scale, Δ , i.e.

$$\epsilon = \beta \Delta \tag{5}$$

The governing equations to be solved (with μ potentially taking into account the molecular and turbulent viscous effects) are:

$$\partial u_i / \partial x_i = 0 \tag{6}$$

$$\rho(\phi) \frac{\partial u_i}{\partial x_j} + \rho(\phi) \frac{\partial}{\partial x_j} (u_i u_j) = - \frac{\partial p}{\partial x_i} + \frac{\partial}{\partial x_j} (\tau_{ij}) - \sigma K(\phi) \delta(\phi) \frac{\partial \phi}{\partial x_i} + \rho(\phi) g_i$$

where $\tau_{ij} = \mu \left(\frac{\partial u_i}{\partial x_j} + \frac{\partial u_j}{\partial x_i} \right)$

and the curvature is

$$K(\phi) = \nabla \cdot \vec{n} \text{ with } \vec{n} = |\nabla \phi|$$

Here σ is the surface tension, δ a delta function, and $K(\phi)$ the curvature.

● II.1 Reinitialization

If the equation system (1) to (6) is solved, as discussed in the next section, the contours of ϕ , around $\phi = 0$, deform as the phases move. This is illustrated for a bubble in a shear flow field in *figure 4*. When the contours in the vicinity of $\phi = 0$ are no longer parallel to $\phi = 0$, then the distance over which density and viscosity change, and surface tension forces are distributed, become nonuniform, i.e., different at different interface locations. Hence, it is desirable to reinitialize the contours in the vicinity of $\phi = 0$ so that

$$|\nabla \phi|_{\phi=0} = 1 \tag{7}$$

This assures the contours are parallel and the Heaviside and δ functions are approximated over uniform thickness in the vicinity of the interface. Since the level set equation is hyperbolic, there is no problem associated with reinitializing the initial value problem at every time step, if necessary.

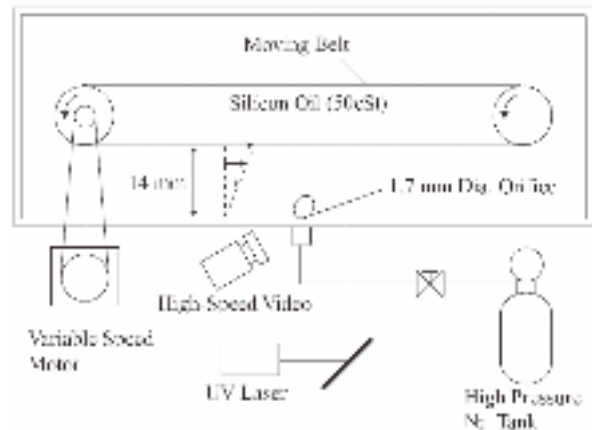


Figure 4: Schematic diagram of the experimental apparatus (Misawa, et al., 1996).

The reinitialization may be accomplished by maintaining the $\phi = 0$ contour and also satisfying (7) by solving

$$\frac{\partial \phi}{\partial \tau} = S(\phi_0)(1 - |\nabla \phi|) + \lambda f(\phi_0) = L(\phi_0, \phi) + \lambda_{i,j,k} f(\phi_0) \quad (8)$$

where ϕ_0 is the distribution to be reinitialized, $S(\phi_0)$ is a sign function, and $\lambda_{i,j,k}$ is a constant for each cell with

$$\lambda_{i,j,k} = \frac{\int_{\Omega_{i,j,k}} H'(\phi_0) L(\phi_0, \phi) d\Omega_{i,j,k}}{\int_{\Omega_{i,j,k}} H'(\phi_0)^2 d\Omega_{i,j,k}} \quad (9)$$

and

$$H'(\phi_0) = \partial H / \partial \phi_0 \quad (10)$$

where $\Omega_{i,j,k}$ denotes the grid cell and τ is a “pseudo” time step.

As we will see in discussing results, this procedure leads to ϕ contours that are parallel to the $\phi = 0$ contour in its vicinity.

● II.2 Solution. Procedure

Many different methods may be used and we briefly consider here those used by Takahira *et al.* (2004). They used a non-staggered grid to discretize the governing equations. As is well known, solution methods for the incompressible N-S equations based on a traditional non-staggered grid, in which all the variables are defined only at the cell center, produce spurious oscillations in the pressure field, i.e., “checker-board” patterns (Patankar, 1980). One of the fundamental causes is that, in a traditional non-staggered grid, a straightforward discretization of the continuity equation does not enforce mass conservation in the cell and causes decoupling of the pressure field. To prevent decoupling, Takahira *et al.* (2004) used a non-staggered grid proposed by Zang *et al.* (1994) and Zang and Street (1995) in which the volume flux is defined on its corresponding face of the cell, in addition to the Cartesian velocity components at the cell center. Although the non-staggered grid was useful in analysis using curvilinear coordinates with high accuracy and a small amount of computer memory, some remedies were needed to apply the non-staggered grid to gas-liquid two-phase flows due to the numerical instability near the interface (Takahira *et al.*, 2004). In the present work, since the application of curvilinear coordinates is not expected, we use a stagge-

red grid for the discretization. We use a semi-implicit time-advancement scheme with the Adams-Bashforth method for the explicit terms and the Crank-Nicholson scheme for the implicit terms. A fractional step method (Projection Method) is used to solve the N-S equations, which involves solution of a pressure Poisson equation. This may be solved using the preconditioned BiCGSTAB (BiConjugate Gradient Stabilized) method (Van der Vorst, 1992, Fujino and Zhang, 1996). ILU decompositions (L is lower triangular and U is upper triangular) were used for the preconditioning. The level-set equation may be solved with the Adams-Bashforth method. The convection terms are discretized with the second-order ENO scheme.

● II.3 Results: Smearred Interface Level Set

Some typical results are shown for level-set simulations of a problem for which there are some experimental results by Misawa *et al.* 1996. The schematic of the experiment is shown in *figure 4*. A shear flow of silicon oil is established, as shown in the figure, and air is injected through the 1.7 mm orifice at the bottom to form bubbles. The problem is quite complex in that the bubble size depends on processes that occur in the work through which the air is injected. Level-set-based simulations have been performed by Takahira *et al.* (2004) for the experimental conditions both at normal gravity (1 g) and the microgravity (0.01 g).

The results indicate that the bubbles start to form necks near the exit of the orifice, as shown in *figure 5*, which also indicates the velocity vectors. This eventually leads to bubble detachment, as shown in the sequences in *figure 6 and 7*, which are shown for 0.01 and 1 g conditions, respectively. Note that gravity acts normal to the wall and assists in detachment, leading to smaller detached bubbles. This is shown clearly in *figures 8 and 9*, which also show in comparison with Misawa *et al.*'s experiments. Table 1 summarizes the Eotvos numbers calculated from the experiments and from the computations where the Eotvos number, E_0 , is given by

$$E_0 = \frac{gD^2(\rho_\nabla - \rho_g)}{\sigma}$$

with the characteristic length D being the equivalent bubble diameter at detachment.

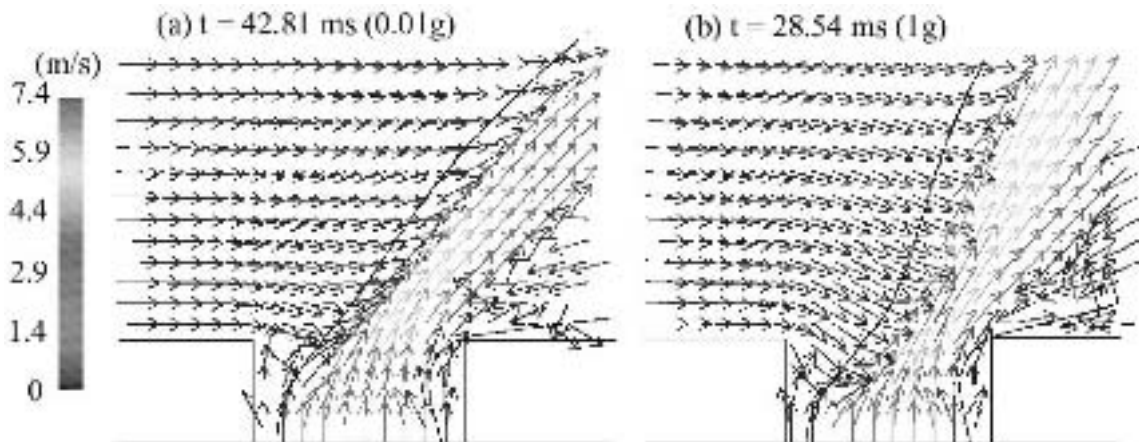


Figure 5: Velocity distribution near an opening when $uw = 0.828$ m/s.

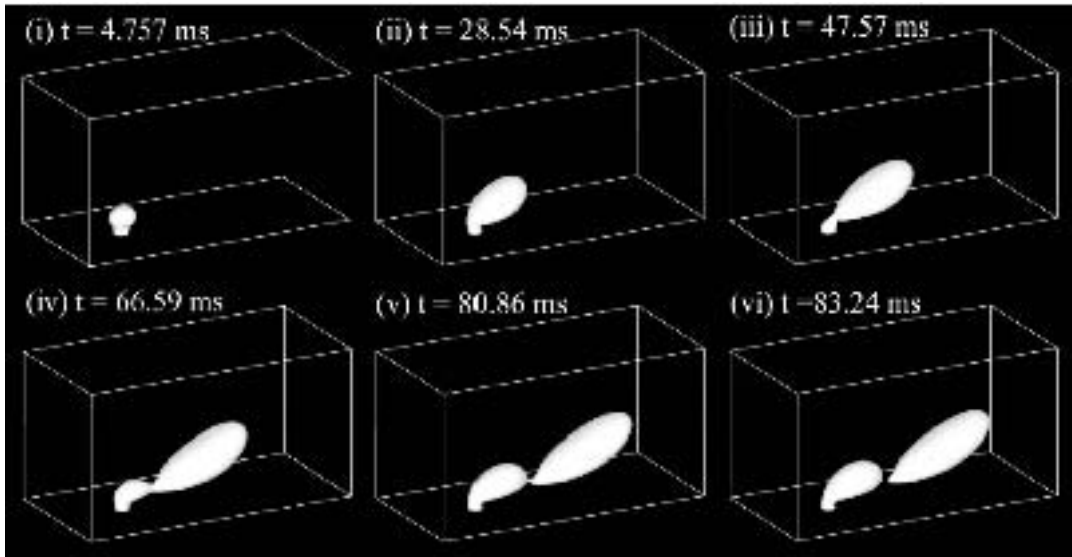


Figure 6: 3D evolution of a bubble injected from an opening when $uw = 0.828$ m/s and the gravity acceleration is 0.01 g.

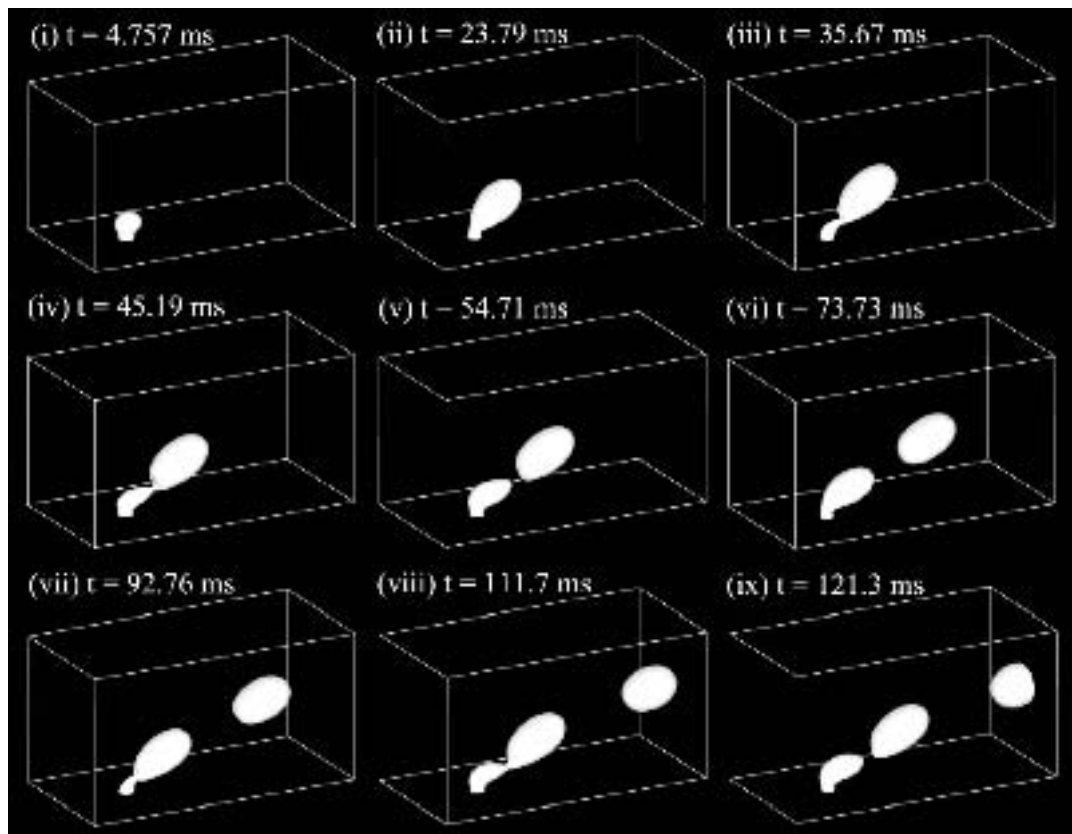


Figure 7: 3D evolution of a bubble injected from an opening when $uw = 0.828$ m/s and the gravity acceleration is 1 g.

Table 1 : Eotvos number of experiments and simulations.

	Gravity acceleration	0.01 g	0.1 g	0.5 g	1 g	
E_0	Exp.	0.148	–	–	10.147	
	Cal.	1st	0.154	1.438	6.001	10.136
		2nd	–	–	–	9.957

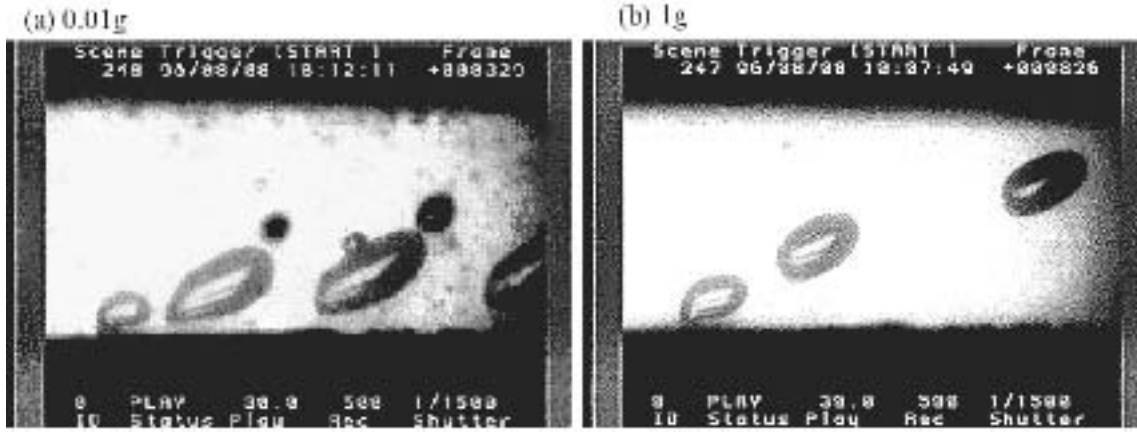


Figure 8: Experimental results on the bubble detachment in a shear flow by Misawa *et al.* (1996). Velocity of moving belt at the top is 0.828 m/s.

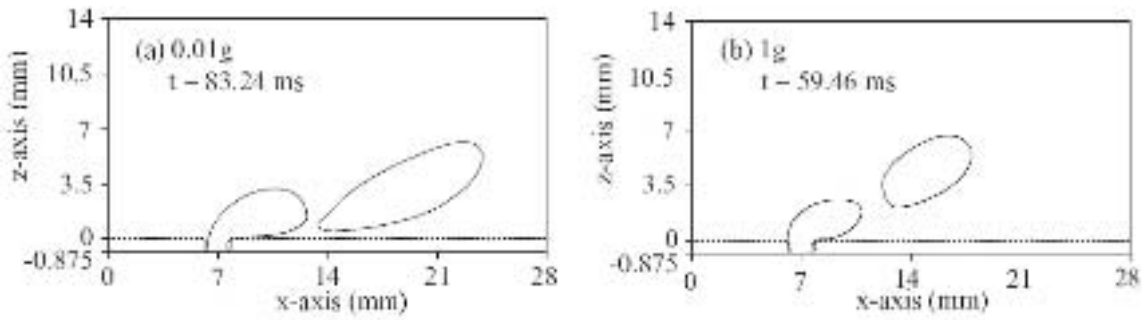


Figure 9: Bubble shape simulated for the experiments by Misawa *et al.* (1996).

These results illustrate the remarkable potential of such direct simulation methods for multiphase flows, in particular simulation of the delicate instability problem that occurs at the orifice exit and leads to bubble detachment. If this effect is improperly modeled, the bubbles in the simulations turn out to be much larger than in the experiments.

● II.4 Sharp Interface. Method and Results

The previous calculations smear the interface over several grid points and result in inaccuracies for problems where length resolution of the interfacial region is desirable. To handle such problems, the fluid density and viscosity is considered to undergo a sudden jump at the interface, requiring the following treatment.

A staggered grid formulation is used to discretize the basic equations where $H(\phi) = 0$ if $\phi \leq 0$ and $H(\phi) = 1$ for $\phi > 0$. Velocity components are defined on cell faces, while the pressure, and level-set function are defined at the center of the control volume. The solver for the Navier-Stokes equation is an evolution of the scheme of Kang *et al.* (2000). We used a semi-implicit time advancement method scheme with Adams-Bashforth method for the explicit terms and a maximization scheme for the implicit terms. A fractional step method (projection method) is used to solve the Navier-Stokes equation. The variable density and viscosity are treated “sharply” and jump conditions are computed using sub-grid linear interpolation based on the level-set function ϕ . The discretized equations for conservation of momentum are,

$$\frac{\vec{V}^{n+1} - \vec{V}^n}{\Delta t} = -\frac{\vec{\nabla} p^{n+1}}{\rho} + \frac{3}{2} \left\{ (\vec{V} \cdot \nabla) \vec{V} + \frac{\vec{F}}{\rho} + \frac{v_{\max}}{2} \vec{M} \right\}^n - \frac{1}{2} \left\{ (\vec{V} \cdot \nabla) \vec{V} + \frac{\vec{F}}{\rho} + \frac{v_{\max}}{2} \vec{M} \right\}^{n-1} + \left\{ \frac{(\nabla \cdot \tau)^T}{\rho} \right\}^n + \frac{v_{\max}}{2} \vec{M}^{n+1} \quad (11)$$

$$\nabla \cdot \vec{V}^{n+1} = 0 \quad (12)$$

Where $\vec{M} = \vec{\nabla}^2(\vec{V})$ and $v_{\max} = \max\left(\frac{\mu_{\text{air}}}{\rho_{\text{air}}}, \frac{\mu_{\text{water}}}{\rho_{\text{water}}}\right)$.

Using the projection method, we define the following fractional steps,

$$\frac{\vec{V}^* - \vec{V}^n}{\Delta t} = \frac{3}{2} \left\{ -(\vec{V} \cdot \nabla) \vec{V} + \frac{\vec{F}}{\rho} - \frac{v_{\max}}{2} \vec{M} \right\}^n - \frac{1}{2} \left\{ -(\vec{V} \cdot \nabla) \vec{V} + \frac{\vec{F}}{\rho} - \frac{v_{\max}}{2} \vec{M} \right\}^{n-1} + \left\{ \frac{(\nabla \cdot \tau)^T}{\rho} \right\}^n + \frac{v_{\max}}{2} \vec{M}^* \quad (13)$$

$$\frac{\vec{V}^{n+1} - \vec{V}^*}{\Delta t} + \frac{\vec{\nabla} p^{n+1}}{\rho} = 0 \quad (14)$$

Assuming that the velocity field at time level $(n+1)$ is divergence-free (9), we derive the variable density pressure Poisson equation,

$$\nabla \cdot \left(\frac{\vec{\nabla} p^{n+1}}{\rho} \right) = \frac{\nabla \cdot \vec{V}^*}{\Delta t} \quad (15)$$

For the example shown, no penetration and no slip conditions at solid wall boundaries, respectively, i.e., $\vec{V} \cdot \vec{N} = 0$, and $\vec{V} \times \vec{N} = 0$. The velocity and normal to the interface is

$$\begin{pmatrix} [\mu u_x] & [\mu u_y] & [\mu u_z] \\ [\mu v_x] & [\mu v_y] & [\mu v_z] \\ [\mu w_x] & [\mu w_y] & [\mu w_z] \end{pmatrix} = [\mu] \begin{pmatrix} \nabla u \\ \nabla v \\ \nabla w \end{pmatrix} \begin{pmatrix} \vec{0} \\ \vec{T}_1 \\ \vec{T}_2 \end{pmatrix}^T \begin{pmatrix} \vec{0} \\ \vec{T}_1 \\ \vec{T}_2 \end{pmatrix} + [\mu] \vec{N}^T \vec{N} \begin{pmatrix} \nabla u \\ \nabla v \\ \nabla w \end{pmatrix} \vec{N}^T \vec{N} - [\mu] \begin{pmatrix} \vec{0} \\ \vec{T}_1 \\ \vec{T}_2 \end{pmatrix}^T \begin{pmatrix} \vec{0} \\ \vec{T}_1 \\ \vec{T}_2 \end{pmatrix} \begin{pmatrix} \nabla u \\ \nabla v \\ \nabla w \end{pmatrix}^T \vec{N}^T \vec{N} \quad (16)$$

where \vec{T}_1 , and \vec{T}_2 are the orthogonal and bi-orthogonal directions to the normal vector \vec{N} . By knowing the value of the jumps across the interface, we can evaluate smoothly the individual derivative to the left and right of the interface. More details on the derivation and discretization of the viscous term are available in Nave (2004).

The momentum equation can then be solved using an approximate factorization technique. We use standard central difference for the Laplacian terms in Eq. (10), WENO 5th order for the convection term, and the technique developed in Kang *et al.* (2000) and Liu *et al.* (1998) for the discretization of the divergence of the rate of strain tensor, τ . For the solution of \vec{V}^* , we solve three tri-diagonal linear systems, one per dimension. As a result, the implicit treatment of the viscous term by the maximization technique lifts the $O(\Delta x^2)$ stability restriction on the time step Δt .

The presence of surface tension in the problem is incorporated into the equation as a jump in pressure across the interface. Thus, the jump condition for the pressure is,

$$[p] - 2[\mu](\nabla u \cdot \vec{N}, \nabla v \cdot \vec{N}, \nabla w \cdot \vec{N}) \cdot \vec{N} = \sigma \kappa \quad (17)$$

where σ is the surface tension, a constant.

Equation (17) is related to the CSF model in which surface tension is incorporated in the momentum equation through the addition of a constant surface force,

$$\vec{F}_{\text{csf}} = \delta(\phi) \sigma \kappa \vec{N} \quad (18)$$

One can show that (17) is consistent with (18) by assuming the level set function is linear around $\phi = 0$, and keeping the leading order term in the expansion about $\phi = 0$ of $\nabla \cdot \left(\frac{\vec{F}_{\text{csf}}}{\rho} + \frac{\nabla \cdot \tau}{\rho} \right)$, the source term in the Poisson equation for pressure.

now denoted by \vec{V} and \vec{N} , rather than \vec{v} and \vec{n} to distinguish them from the level-set calculations with smeared interfaces. This is straightforward to modify for a porous wall by allowing a pressure difference related wall-normal velocity. The pressure boundary conditions at solid wall boundaries are Neumann, $\vec{\nabla} p \cdot \vec{N} = 0$.

In the sharp interface or ghost fluid method (GFM), the treatment of property discontinuities at the interface gives rise to the specification of jump conditions for the diffusion term in the momentum equation (13), and in the Poisson equation (15). Following the notation in Kang *et al.* (2000) we denote the jump across the interface by $[\cdot]$, we compute the matrix of derivative jumps due to the discontinuity in viscosity,

The interface is tracked using the level-set equation,

$$\frac{\phi^{n+1} - \phi^n}{\Delta t} + \vec{V}^{n+1} \cdot \vec{\nabla} \phi^n = 0 \quad (19)$$

with WENO 5th order being used to discretize $\vec{\nabla} \phi^n$.

The variable coefficient Poisson equation (15) is solved with the interface jump condition defined by (17). The discretization closely follows that described in Liu *et al.* (1998). In order to compute curvature around the interface, we use subgrid linear interpolation,

$$\kappa_{\text{Int}} = \theta \kappa_{\text{Left}} + (1 - \theta) \kappa_{\text{Right}} \quad (20)$$

Where θ is the cut cell size,

$$\theta = \frac{|\phi_{\text{Left}}|}{|\phi_{\text{Left}}| + |\phi_{\text{Right}}|} \quad (21)$$

This discretization produces a linear system $Ax = b$ to be solved. Since the matrix A is poorly conditioned, solving for pressure requires roughly 80% of the computational time. As a result, the solution method needs to be complemented by a preconditioner in order to limit the number of iterations required.

We use the BiCG-Stab iterative method from Van der Vorst (1992) along with an Incomplete Upper-Lower (ILU) preconditioner, Axelsson (1994). Boundary conditions for most problem of interest here have solid walls in x and z directions and air inflow/outflow or in some cases periodic in the y -direction.

The entire solution scheme (tab. 2), corresponding to an Euler step, with the exception of the reinitialization is then embedded in the 3rd order Runge-Kutta TVD scheme (See Nave (2004) for details) from Shu *et al.* (1988),

$$\vec{V}^{n+1} = \frac{1}{3}\vec{V}^n + \frac{2}{3}E\left(\frac{3}{4}\vec{V}^n + \frac{1}{4}E(E(\vec{V}^n))\right) \quad (22)$$

Table 2: Solution scheme for 1 Euler step, $E(V)$.

Solve (11) for \vec{V}^*
 Solve (13) for P^{n+1}
 Solve (12) for \vec{V}^{n+1}
 Solve (17) for ϕ^{n+1}

We will now illustrate the typical results of the GFM calculations outlined above to scalar transfer to a liquid film falling under normal gravity. First, we illustrate in *figure 10* the wave structure at $Re = 69$, where Re is the film Reynolds number based on average film thickness and velocity. In *figure 11a* we show the flow patterns (streamlines) moving with the wave. The recirculation within the wave creates stagnation points which are convergent (A) and divergent (B). This recirculation pattern considerably enhances mass and heat transfer at the gas-liquid interface.

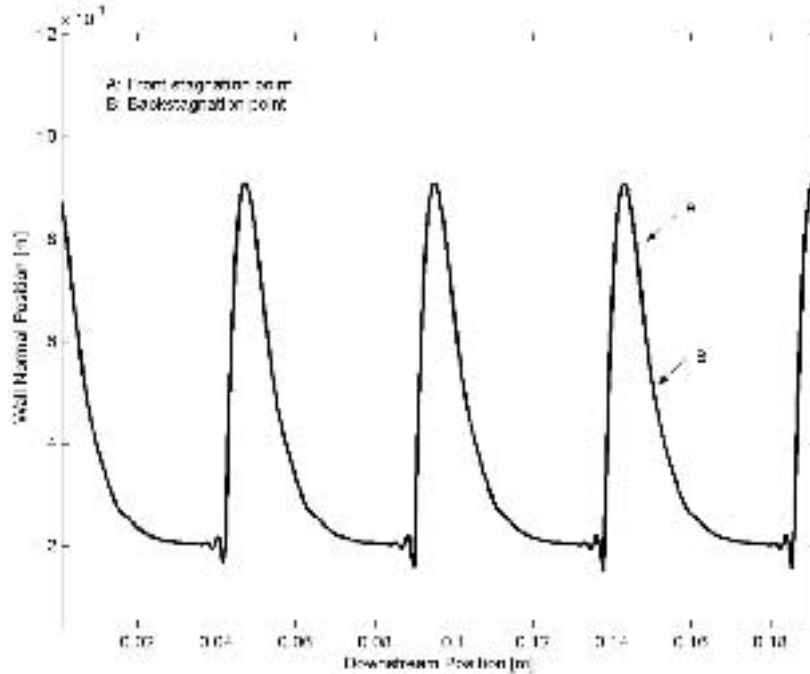


Figure 10: Interfacial wave structure for a gravity-driven water film at $Re = 69$. There is a recirculation pattern in the wave, shown in Fig.2, which gives rise to the A and B stagnation points. The vertical axis is enlarged in comparison to the horizontal to illustrate the wave structure clearly.

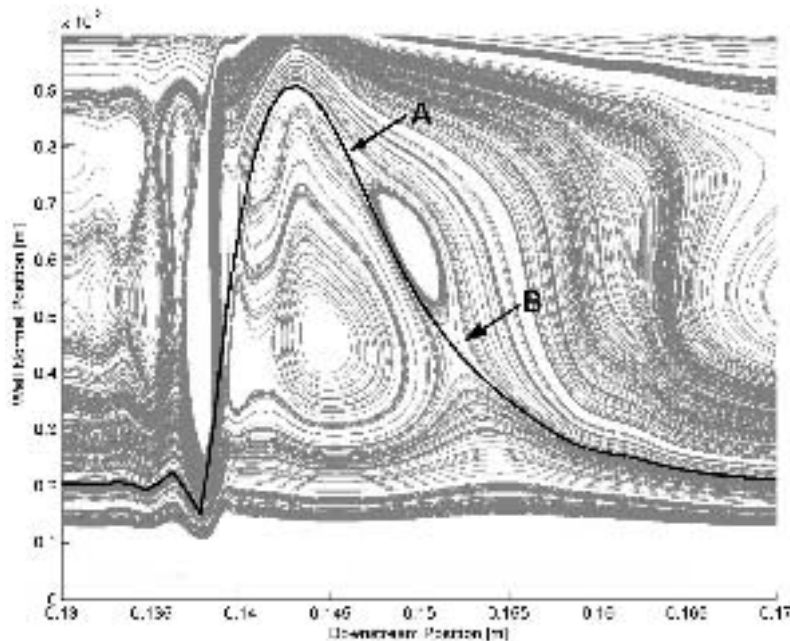


Figure 11a: Streamlines for one wave in the frame moving with the wave celerity at $Re = 69$.

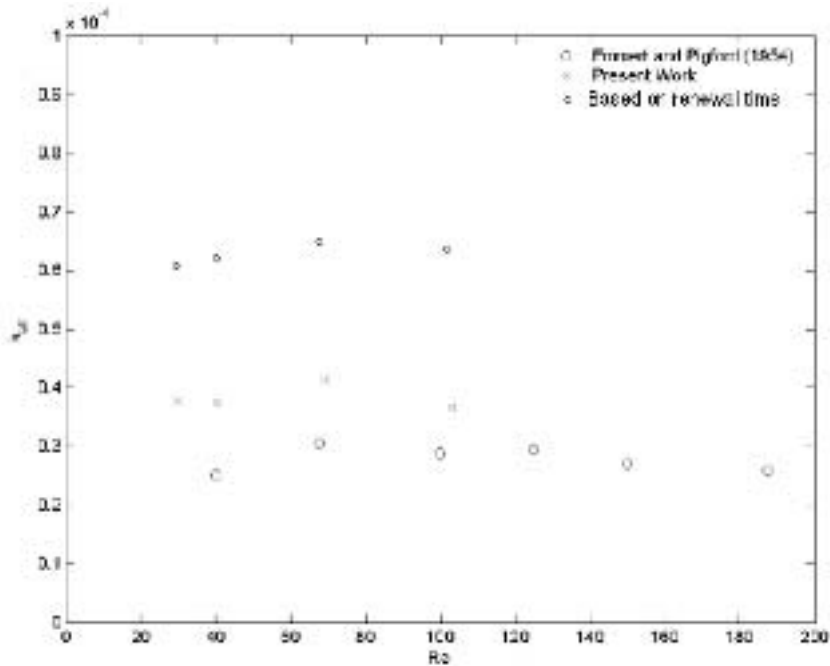


Figure 11b: Comparison of computation and experiments of Emmert and Pigford (1954) for the average mass transfer coefficient vs. $Re - D = 1.95 \cdot 10^{-9} \frac{m^2}{s}$.

In *figure 11b*, we compare scalar transfer rates to the results of Emmert and Pigford (1954). The upper limit of the transfer rates can also be roughly estimated based on a “renewal” time based on the time a particle emerging from the divergent stagnation point B takes to get to the convergent stagnation point, A. Clearly this rough estimate, which is based on penetration theory, is not as accurate as the full solution of the coupled concentration equations.

We now consider briefly calculations of free-surface interactions with wall turbulence. The physical situation is one in which a liquid film flows rapidly at supercritical conditions, along a flat plate. Ultimately, this film will slow down due to friction to velocities equal to that of the gravity wave and undergo a hydraulic jump, but the conditions considered are in

advance of such a jump, so the film is rather smooth and there is intense turbulence generation at the bottom wall. Such problems, for example, are encountered in dam sluices. In any case, *figure 12* shows the interfacial configuration due to turbulent structures impinging on the free surface from the bottom. The bumps are clearly discernible, and in *figure 13* the underlying turbulence structures are visualized by using vortex markers. It is clear that the quasi streamwise vortices, which are seen in wall turbulence, are also discernible here. However, they give rise to bursts and ejections, which then impinge on the interface and cause the bumps shown in *figure 12*. The vertical scale is enlarged in these visualizations in order that the structures can be clearly seen, and for this reason they are somewhat distorted in the vertical direction.

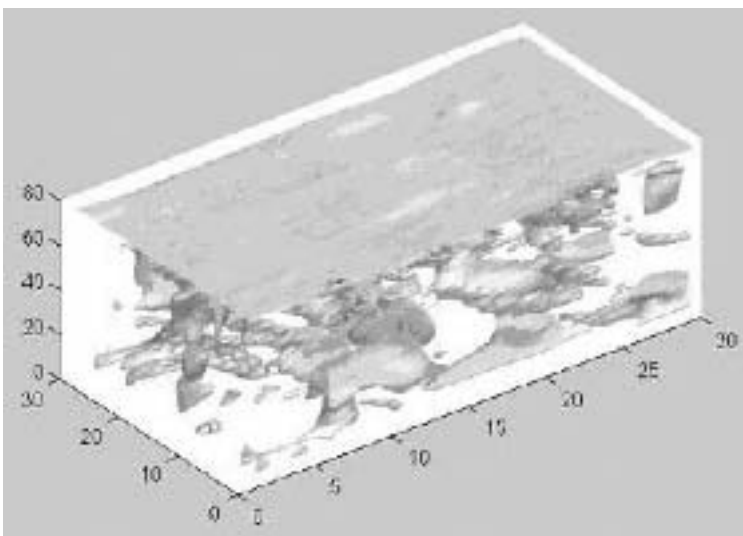


Figure 12: Direct numerical simulation of a supercritical liquid film using the level-set/ghost-fluid method. The free surface shows bumps developing from impinging turbulence structures, which are shown as the vortical elements below the surface. The vortical elements are identified by various techniques, including isopressure surfaces. The vertical coordinate is enlarged to show the subsurface structures.

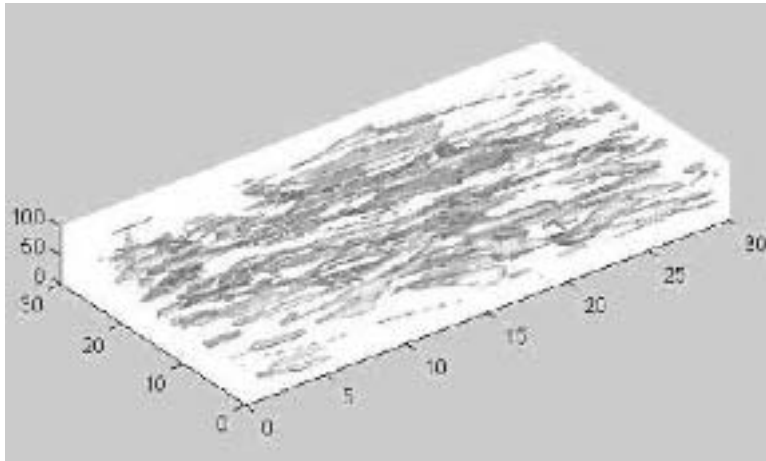


Figure 13: The same flow as in Figure 12 but with the vertical dimensions of the correct proportion. The vortical structures shown are similar to those found in wall turbulence, i.e., quasi-streamwise vortices.

III ■ PHASE FIELD METHODS

An alternative to considering the interface between phases as a contact discontinuity is to actually model it based on consideration of interfacial forces. Many excellent reviews of the subject are available (see Bray (1994) and Langer (1992)). The main applications have been to systems where convective effects are unimportant, e.g. quenching from a disordered phase to an ordered phase. The ordered region length scales grow with time, and a network of domains of the equilibrium phases develops. An example is the spinodal decomposition of binary alloys or phase separation of simple fluids quenched below the mixture critical point. In principle, a wide variety of problems can be addressed, including the behavior of emulsions, polymer melts, coalescence, wetting, nucleation, etc. Problems in which convective effects are important, e.g. spinodal decomposition in shear fields, have received very little attention — perhaps because of the difficulty of solving the coupled phase-field and fluid motion equations. Some early results are discussed here, as such methods are at the most interesting edge of multiphase systems research today.

The early work grew out of magnetization of the Ising model, and the terminology derives from this, but one should not be put off by jargon! The continuum description proceeds in terms of the coarse-grained “order-parameter” field (e.g. the magnetization density, concentration or some such), $C(\vec{x}, t)$. We take this to be a scalar field, but in fact it does

not have to be. For example, nematic liquid crystals can be described by tensor order parameters that are invariant under a certain local transformation. In any case, for scalar order parameters we may define a Landau free-energy function $A[C]$ as

$$A[C] = \int_{\Omega} \{ \beta \chi(C) + 1/2 \alpha |\nabla C|^2 \} \quad (23)$$

where the potential $\chi(C)$ is the homogeneous free energy which is often described by a double well potential, as shown in figure 14. For example, we could put

$$\chi(C) = (1 - C^2)^2 \quad (24)$$

with minima occurring at $C = \pm 1$. The two minima correspond to the two equilibrium states. The $|\nabla C|^2$ term is called the gradient free energy and associates an energy cost where C changes rapidly, i.e. at the interface between the phases. The parameters, α and β can be scaled out using “surface tension”, σ , and “interface thickness”, ξ , where

$$\sigma \propto \sqrt{\alpha\beta} \quad \text{and} \quad \xi \propto \sqrt{\alpha/\beta} \quad (25)$$

When time variation is absent, i.e. at equilibrium, $A[C]$ should be a minimum with regard to variations of C , i.e.

$$\frac{\delta A}{\delta C} = \beta \chi'(C) - \alpha \nabla^2 C = 0 \quad (26)$$

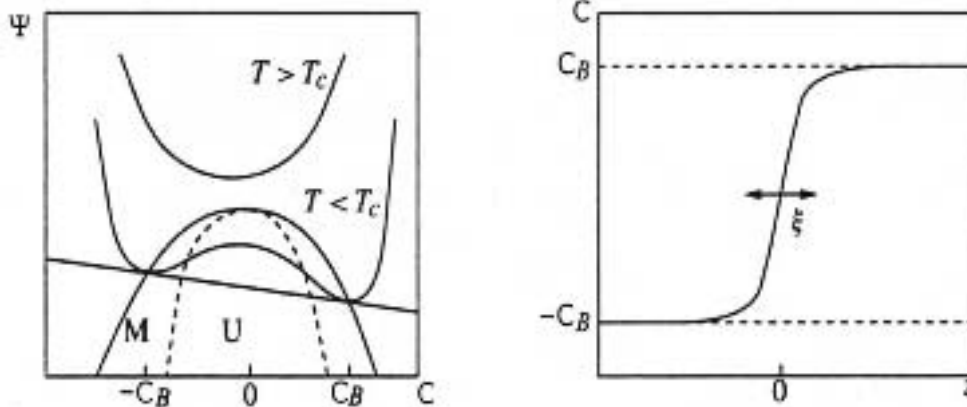


Figure 14: Schematic picture of the homogeneous specific free energy Ψ as a function of C (left) and the equilibrium interface profile (right).

If the order parameter is not conserved, then time evolution is

$$\frac{\partial C}{\partial t} = -k[\beta\chi' - \alpha\nabla^2 C] \quad (27)$$

called the Landau-Ginzburg model.

There is significance to this model for the Ising model and alloys that go through order-disorder transitions rather than phase separating.

When the order parameter is conserved, we get

$$\frac{\partial C}{\partial t} = \nabla \cdot \left(M\nabla \frac{\delta A}{\delta C} \right) = \nabla \cdot \{M\nabla [\beta\chi'(C) - \alpha\nabla^2 C]\} \quad (28)$$

The divergence assures conservation. M is related to a “mobility” or diffusion. The quantity in square brackets is the chemical potential $\mu \equiv \delta A / \delta C$. This is the Cahn-Hilliard equation, and combined with the Navier-Stokes system, called Model H (see Bray).

For convective systems, the order parameter is transported by fluid motion, so we have (for constant M)

$$\frac{\partial C}{\partial t} + \vec{u} \cdot \nabla C = M\nabla^2 \mu \quad (29)$$

and

$$\frac{\partial(\vec{u}\rho)}{\partial t} + \vec{u} \cdot \nabla(\vec{u}\rho) = \eta\nabla^2 u - \nabla p - C\nabla\mu \quad (30)$$

where η – viscosity and ρ is density. If $\rho = \rho(C)$, then

$$\nabla \cdot \vec{u} = -\frac{M}{\rho(C)} \frac{\partial \rho}{\partial C} \nabla^2 \mu \quad (31)$$

i.e., the velocity field is not divergence free in the interface region. Note that the surface tension effect is captured by the $C\nabla\mu$ term in the momentum equation.

We turn now to some applications of the Cahn-Hilliard equation, compared to the level-set equations, it assumes conservation of the order-parameter (mass, if C is concentration). The equation can be used in several different ways. The first is to simply use C as a marker function. This is much like the level-set method, but with the added benefit that mass is conserved. The interface can be made as sharp as desired, or can be tolerated by the numerical procedures.

To proceed, we show in *figure 15* calculations for splashing of a liquid drop into a deep pool of water and a Rayleigh-Taylor instability. The thickness of the interface remains relatively constant, and the results are very similar to what would be obtained with level-set calculations.

The second area of application is to problems where the physics of the interfacial processes is of importance. *Figure 16* shows one such problem in which drops are coalescing. *Figure 17* shows phase separation of a binary mixture under shear, and *figure 18* the same problem in 3D. The string-like structures have been seen by Hashimoto *et al.* (1995). Note that the 2D calculations show “plate” formation, whereas the 3D calculations show string formation. These results are of great interest for separation of binary mixtures.

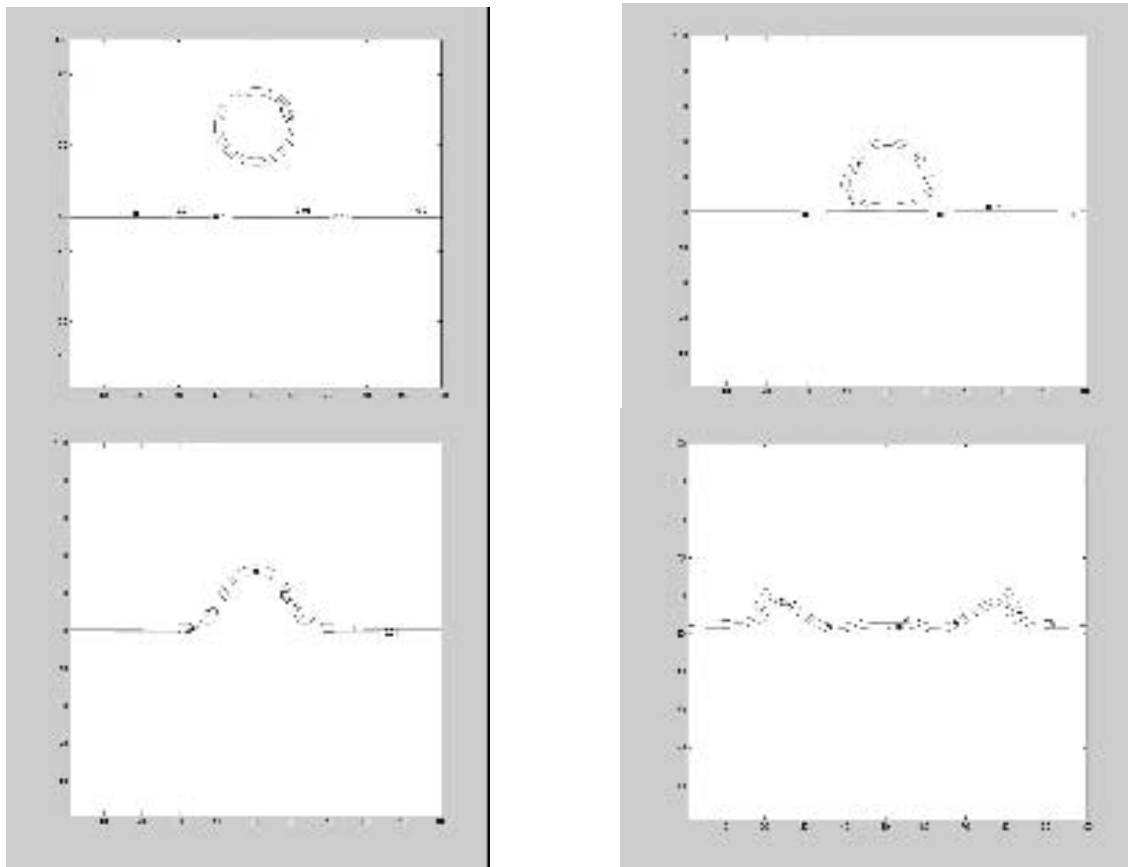


Figure 15a: Splashing of a water drop in a deep water pool.

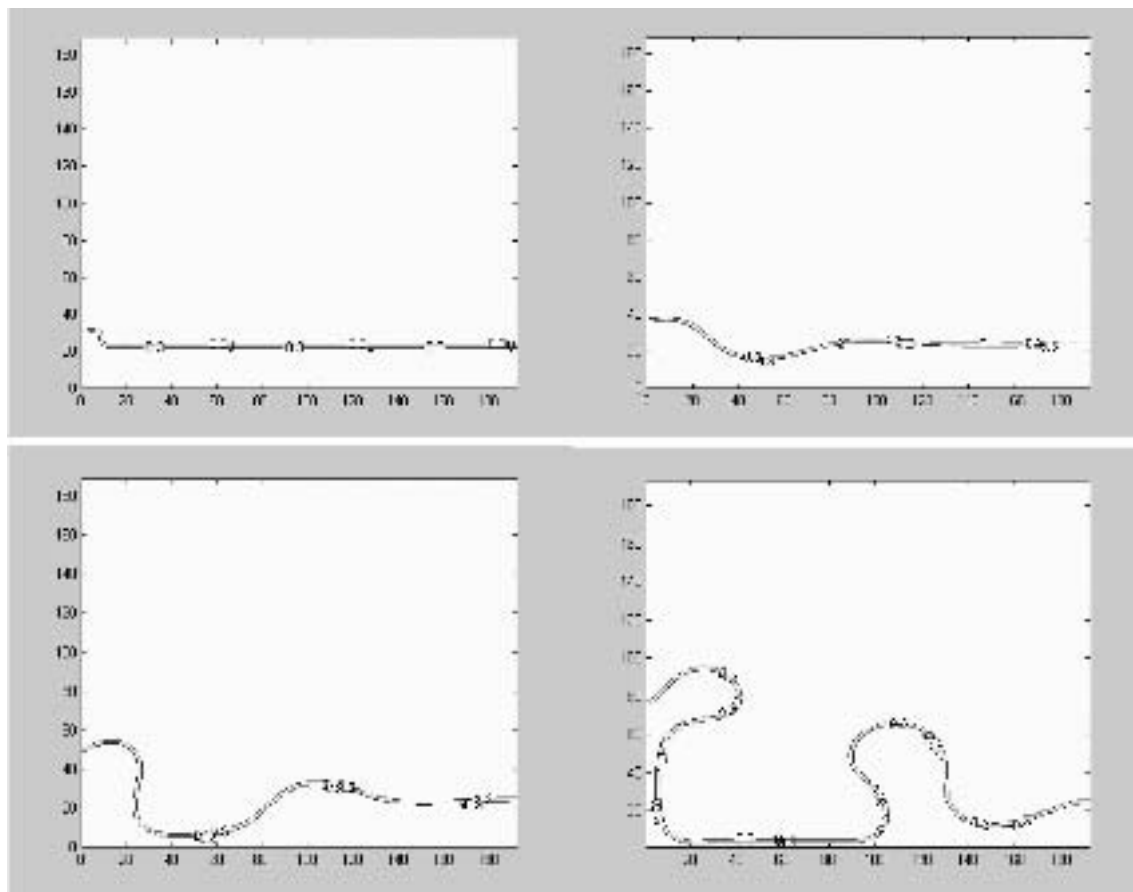


Figure 15b:

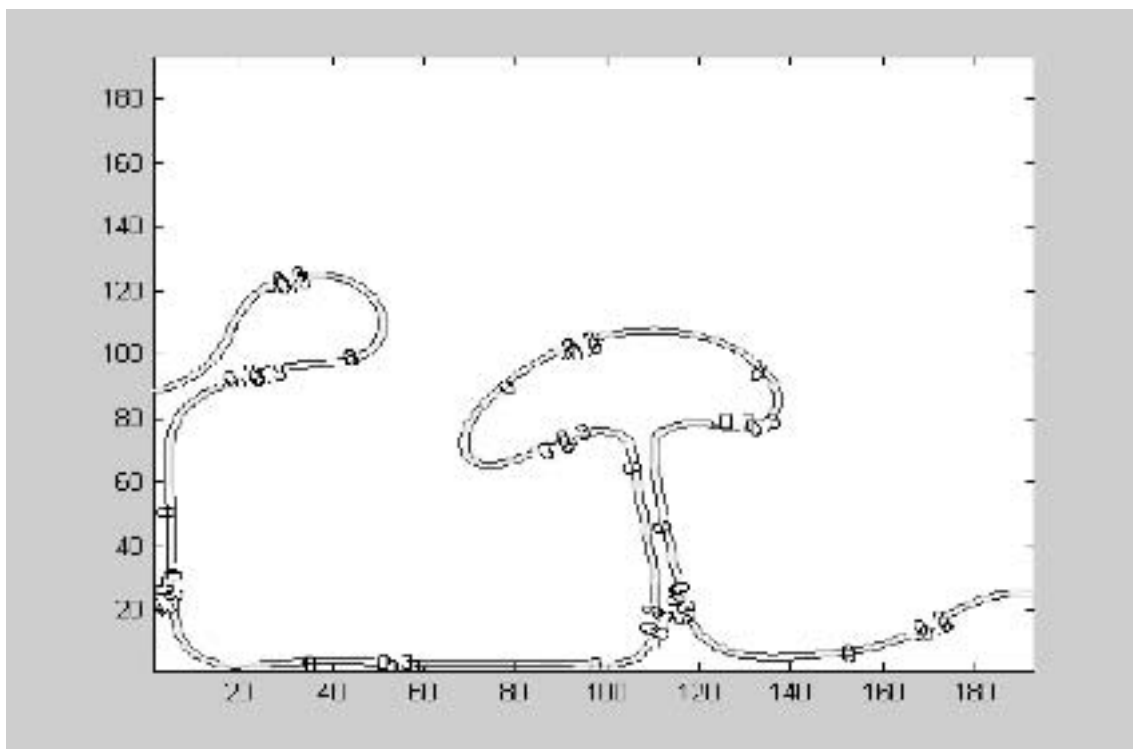


Figure 15c: A Rayleigh-Taylor instability.

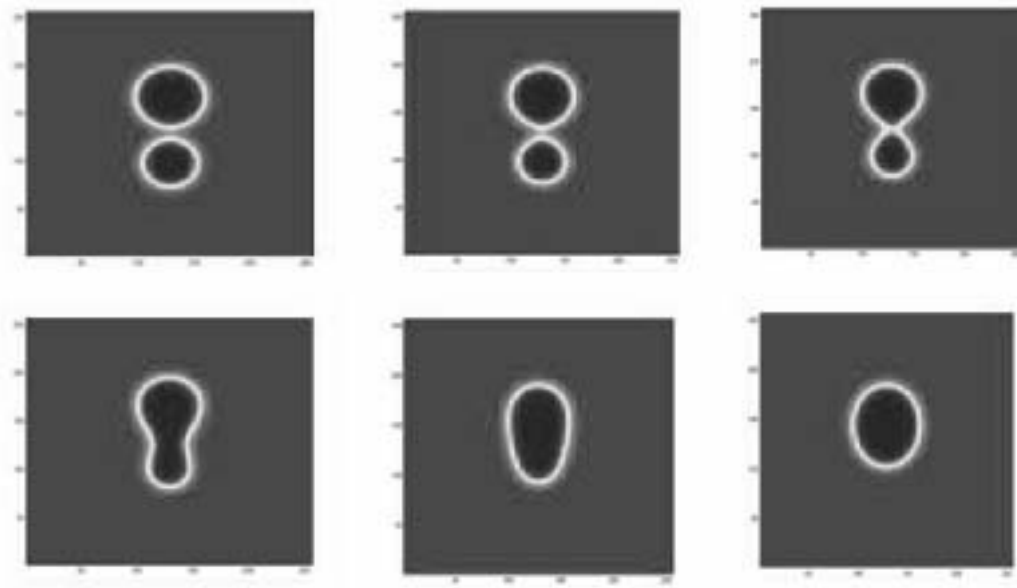


Figure 16: Coalescence of drops ripening.

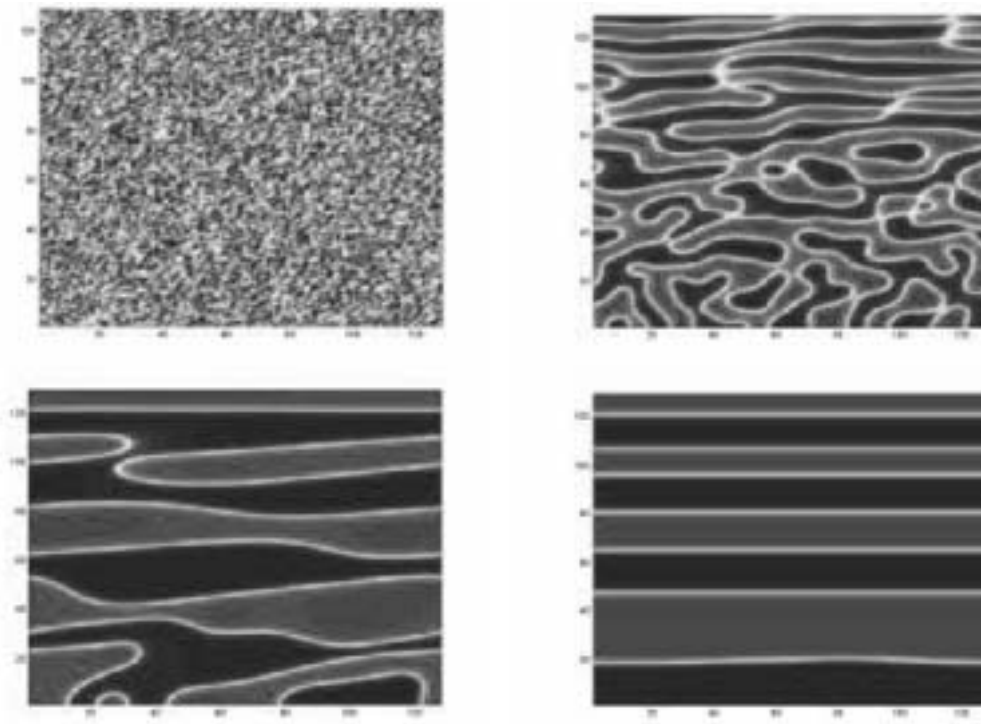


Figure 17: 2D phase separation under shear from homogeneous initial conditions.

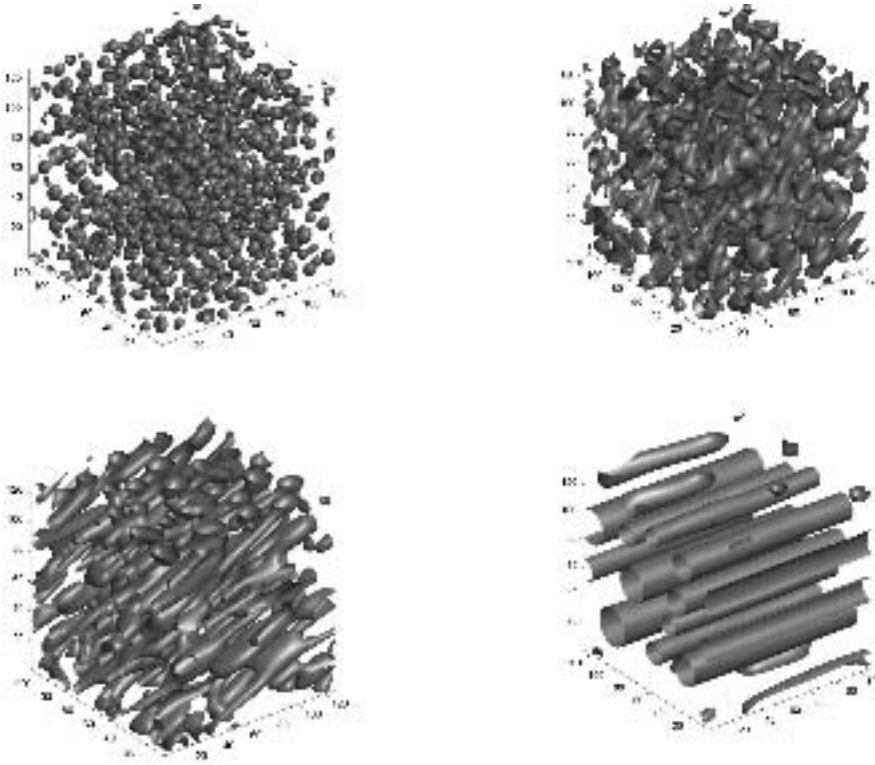


Figure 18: 3D phase separation under shear.

IV ■ TWO-FLUID VISCOELASTIC MODELS

● IV.1 Introduction

Descriptions of phase separation are usually classified into a solid diffusional model (called Model B) and a fluid model (Model H). In the former, diffusion is the only transport process whereas in the latter, material is transported by both diffusion and hydrodynamic flow. Recently, quite unusual phase separation was found in polymer systems having intrinsic dynamic asymmetry between the components i.e. composed of fast and slow components. This “dynamic asymmetry” can be induced by either the large size difference or a difference in the glass-transition temperature between the components of a mixture. The former can often exist in complex fluids such as polymer solutions, micellar solutions, colloidal suspensions, emulsions and protein solutions. The latter can exist in any mixture in principle. The effect of the asymmetry is to cause a strong kinetic coupling between the stress field and the concentration fluctuation. So this new type of phase separation is called “viscoelastic phase separation” since viscoelastic effects play an important role.

● IV.2 Model

Consider a fluid mixture of Components 1 and 2. Component 1 is the “hard” component, and component 2 is the “soft” one. The former would correspond to the polymer component in the case of a polymer solution and the latter to the solvent. Let $v_1(r,t)$ and $v_2(r,t)$ be their respective average velocities and $\phi(r,t)$ be the volume fraction of the component 1 at point r and time t . The two components are assumed to have the same density — for simplicity.

Then, the conservation law gives

$$\frac{\partial \phi}{\partial t} + v \cdot \nabla \phi = - \nabla \cdot [\phi(1-\phi)(v_1 - v_2)] \quad (32)$$

The volume-averaged velocity v is taken to be divergence free and is given by

$$v = \phi v_1 + (1-\phi)v_2 \quad (33)$$

The free energy of the system F_{mix} is given by

$$F_{\text{mix}} = f(\phi) + \frac{c}{2} (\nabla \phi)^2 \quad (34)$$

Defining the osmotic stress tensor π as

$$\nabla \cdot \Pi = \phi \frac{\delta F_{\text{mix}}}{\delta \phi} \quad (35)$$

From the component momentum equations and (2), the conservation law for the average velocity v is

$$\rho \frac{\partial v}{\partial t} = - \nabla \cdot \Pi + \nabla p + \nabla \cdot \sigma + \eta_S \nabla^2 v \quad (36)$$

σ

where η_S is the stress tensor for the hard component, and η_S

ζ

the solvent viscosity. Here the advective term has been dropped as inertial terms do not become important until very late stages. The temporal term is also dropped during numerical implementations for the same reason.

Also under the quasi-stationary approximation,

$$v_1 - v_2 = - \frac{1-\phi}{\zeta} [\nabla \cdot \Pi - \nabla \cdot \sigma] \quad (37)$$

Here ζ is a friction coefficient.

For stress, the equation is modeled based on Maxwell's stress equation.

$$\sigma_{ij} = \int_{-\infty}^t dt' [G_S(t-t')\kappa^{ij}(t') + G_B(t-t')(\nabla \cdot v_1(t'))\delta_{ij}] \quad (38)$$

where
$$\kappa^{ij} = \frac{\partial v_1^i}{\partial x_i} + \frac{\partial v_1^j}{\partial x_j} - \frac{2}{d} (\nabla \cdot v_1)\delta_{ij} \quad (39)$$

The velocity dependence is only on component 1 since the stresses are assumed to be generated only in the hard component. G_S and G_B are material functions, and are called the shear and bulk relaxation moduli, respectively.

The effect of elastic stresses on the soft component can also be incorporated in a similar manner by using separate stress equations for it.

It is interesting to note that the simple fluid model (Model H) can be recovered from this "general" approach by putting the stresses equal to zero.

● IV.3 Evolution

Viscoelastic phase separation is characterized by unusual phase-separation behaviors. They include the moving droplet phase, which coarsens unusually slowly, and the phase-

inversion phenomena in the late-stage of phase separation. Such behaviors are never observed in conventional phase separation. In particular, network-like phase separation is interesting since a minority phase can transiently form a continuous phase here. The phenomenon has a technological importance, since it enables us to intentionally form the continuous network-like structure of a minority phase.

It proceeds as follows:

Just after a temperature quench, a transient gel is formed.

The polymer rich phase, which is thermodynamically a majority phase, is selectively nucleated after some incubation time.

The polymer rich phase shrinks as chemical gel shrinks.

In the final stage, the network-like structure of the polymer rich phase I transiently formed.

In the final stages, the network-like structure relaxes to circularly isolated domains.

In this way, phase inversion takes place in this phase separation. It is obvious that there is no self-similarity and no dynamic scaling for the pattern evolution of viscoelastic phase separation.

The bulk stress in equation (39) is introduced to express the formation of a transient gel right after the initiation of phase separation in the "dynamically asymmetric" mixture and suppresses concentration fluctuations in the polymer rich phase selectively. It is known to be important in the volume shrinking behavior of gels that is observed during such phase separation.

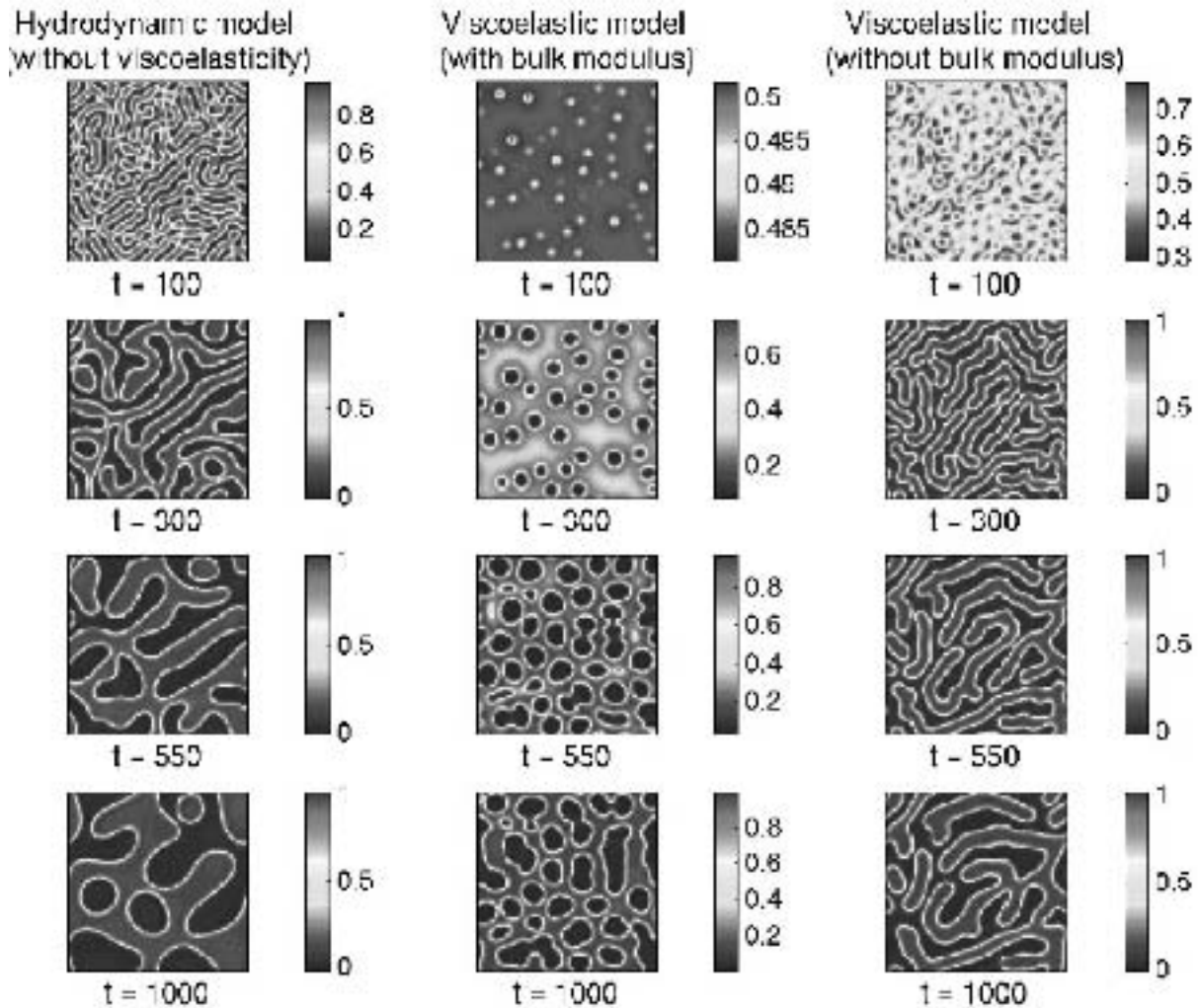


Figure 19: Comparison of time evolutions for the simple fluid model and the viscoelastic model (with and without bulk moduli) for a 50:50 mixture.

Figure 19 shows a comparison of time evolutions for the simple fluid model and viscoelastic model (with and without bulk moduli). The formation of solvent droplets followed by a network-like structure of the polymer rich phase is observed only in the viscoelastic case with bulk moduli. Since this is a 50:50 case, phase inversion occurs at very late stages and so is not observed in this simulation. The case of o

coelastic phase separation without the bulk moduli is similar to the simple fluid model but has slower dynamics.

Figure 20 shows phase inversion for a 30:70 case. Solvent droplets form initially, followed by a transient network that breaks up to form polymer droplets.

Figures 21 and 22 show the effect of shear on the case from figure 19. For the lower shear rate 0.01, the early stages are not significantly affected by the applied shear. At

Viscoelastic phase separation for a 30:70 case showing phase inversion

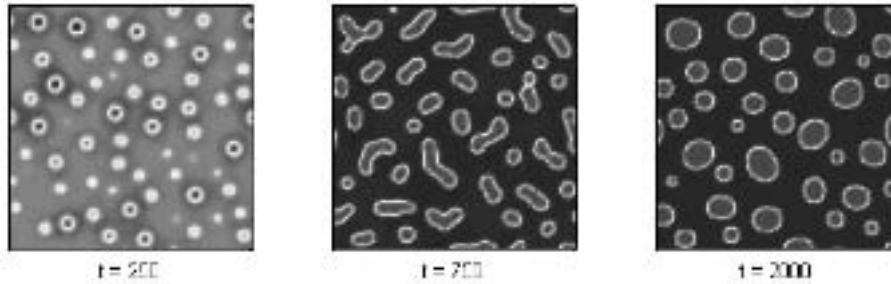


Figure 20: Phase inversion in the 30:70 case for Viscoelastic phase separation.

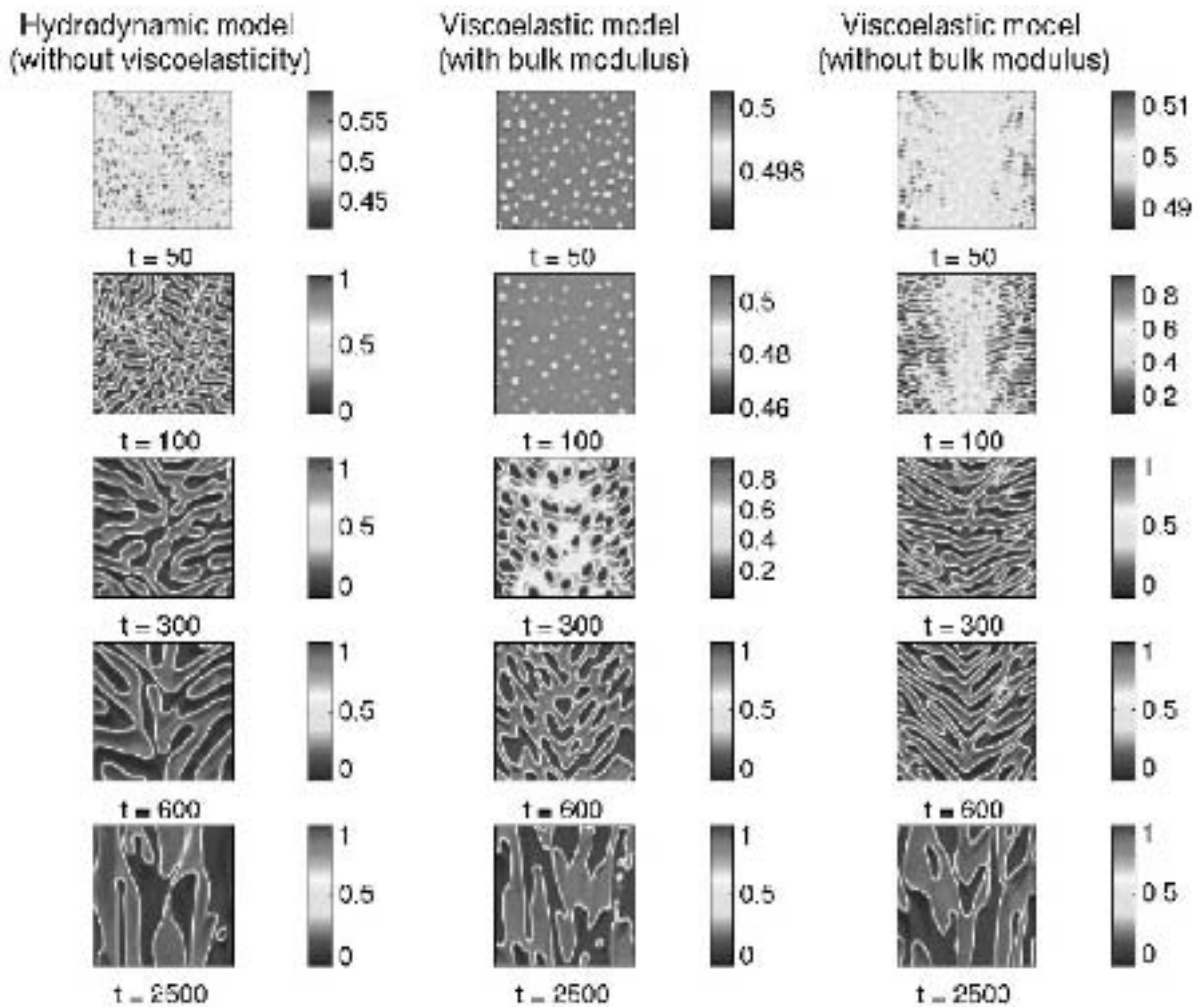


Figure 21: Comparison of phase separation for the 50:50 case under shear (shear rate 0.01).

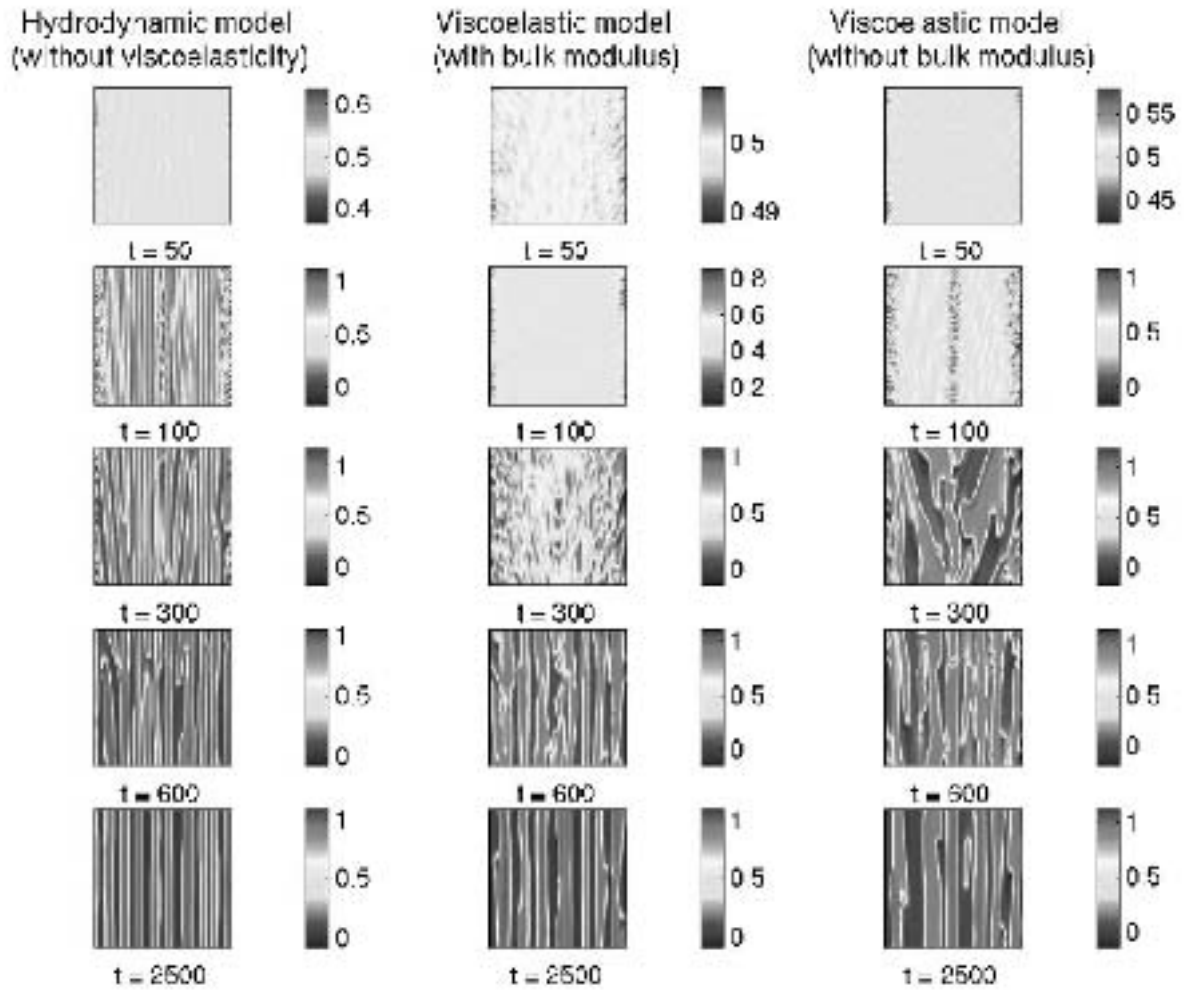


Figure 22: Comparison of phase separation for the 50:50 case under shear (shear rate 0.1)

late stages there is an underlying tendency of the domains to align in the direction of the shear. Network formation of the polymer rich phase is still observed in the viscoelastic case with bulk moduli. For the higher shear rate 0.1 in *figure 22*, shear effects dominate the internal dynamics and the domains align to form stringy patterns in this case. For the simple fluid case, this process is fast whereas for the viscoelastic case the intermediate case is characterized by chaotic motion of the domains. The width of the lamellae at the last stage is found to be larger for the viscoelastic case.

attention to melts of flexible polymers that are composed of two chemically distinct types of monomers, denoted A and B. Polymers are described by space curves $R(s)$, where $s \in (0, N)$ is a chain contour parameter and N denotes the total contour length of the polymer. As shown in *figure 23* for an AB diblock copolymer, $R(s)$ with $0 < s < fN$ describes the positions of the type A monomers, while $R(s)$ with $fN < s < N$ describes the positions of the monomers on the type B block. ff denotes the fraction of type A monomers on the copolymer, i.e. its composition.

V ■ SELF-CONSISTENT FIELD THEORETIC METHODS

● **V.1 Theoretical Aspects**

We follow here the methodology for constructing statistical field theory models of inhomogeneous polymeric fluids described by Ganesan and Fredrickson (2001), and Fredrickson (2002). In the present work, we will restrict our



Figure 23: Schematic showing AB copolymer chain and notation.

From the instantaneous configurations of a collection of n block copolymers, we can define “microscopic” density and elastic stress operators, e.g. for species A

$$\hat{\rho}_A(r) = \sum_{\alpha=1}^n \int_0^{fN} ds \delta(r - R_\alpha(s)) \quad (40)$$

$$\nabla \cdot u = 0$$

$$= \frac{3}{b^2} \sum_{\alpha=1}^n \int_0^{fN} ds \frac{dR_\alpha(s)}{ds} \frac{dR_\alpha(s)}{ds} \delta(r - R_\alpha(s)) \quad (41)$$

where b is the statistical segment length (typical monomer size). The microscopic density $\hat{\rho}_A(r)$ is a scalar field, while the microscopic elastic stress $\hat{\sigma}_A(r)$ is a symmetric second-rank tensor field. Similar expressions hold for the density and stress fields of the B monomer species.

$$U_0[R] = \frac{3}{2b^2} \sum_{\alpha=1}^n \int_0^{fN} ds \left| \frac{dR_\alpha(s)}{ds} \right|^2 \quad (42)$$

Next, we turn to consider the potential energy model. The *intramolecular* potential energy of a collection of n polymers can be written as in (42).

If the A and B monomers have comparable sizes, then this formula holds regardless of the specific polymer architecture (i.e. diblock, triblock, or pentablock). The simplest model of *intermolecular* interactions in an A-B melt enforces *incompressibility* with a local constraint

$$\prod_r \delta(\hat{\rho}_A(r) + \hat{\rho}_B(r) - \rho_0), \quad (43)$$

where ρ_0 is the total (constant) monomer density. Dissimilar monomer contacts are penalized by means of a potential energy contribution

$$H[\phi_A, \mu_A, \mu_B] = -n \ln Q[\mu_A, \mu_B] + \rho_0 \int dr [\chi \phi_A (1 - \phi_A) - \mu_A \phi_A - \mu_B (1 - \phi_A)] \quad (45)$$

The functional Q is the partition function of one block copolymer experiencing inhomogeneous chemical potential fields μ_A and μ_B that exert forces on the A and B blocks, respectively. Q can be computed deterministically by means of the formula:

$$Q[\mu_A, \mu_B] = \frac{1}{V} \int dr q(r, N; [\mu_A, \mu_B]), \quad (46)$$

$q(\mathbf{r}, s)$ appearing in this equation is a propagator describing the statistical weight that a piece of chain with contour length s has its end at position \mathbf{r} . This object can be computed by a Feynman-Kac formula for the copolymer path integral

$$\frac{\partial}{\partial s} q(r, s) = -\mu(r, s)q(r, s) + \frac{b^2}{6} \nabla^2 q(r, s) \quad (47)$$

$$U_1[R] = (\chi/\rho_0) \int dr \hat{\rho}_A(r) \hat{\rho}_B(r), \quad (44)$$

where $\chi > 0$ is the “Flory chi parameter”, which describes the strength of A-B monomer repulsions. Increasing χ can thus drive a local phase separation between A and B segments. The connectivity of the A and B blocks prevents a macro-phase separation of A and B — such phase separation would require significant chain deformation and the decreased configurational entropy of the polymers would produce a large “elastic energy” contribution that would be manifest in the value of U_0 . Instead, phase separation takes place to create composition patterns with 1-100 nm domains, which at equilibrium reflect a balance between the competing tendencies for minimal chain stretching and minimal A-B contacts, while maintaining overall melt incompressibility.

As described by Fredrickson [2002], the configurational partition function $Z = \int \ominus[R] \exp(-U_0[R] - U_1[R])$,

where $\int \ominus[R]$ denotes n path integrals over the polymer configurations, can be converted exactly into a statistical field theory. In this theory, the polymer coordinates are integrated out, leaving functional integrals over fluctuating density fields, ρ_A and ρ_B and two conjugate fluctuating chemical potential fields μ_A and μ_B . The incompressibility constraint can be used to eliminate ρ_B in favor of ρ_A , resulting in three independent fields: μ_A , μ_B , and $\phi_A(r) = \rho_A(r)/\rho_0$, the volume fraction of type A segments. An extended version of the theory [5] retains also fluctuating elastic stress, σ_A and σ_B , and conjugate elastic strain fields, ε_A and ε_B . Here we present only the simplest version without the elastic fields. The transformed partition function can be written $Z = \int \ominus[\phi_A] \int \ominus[\mu_A] \ominus[\mu_B] \exp(-H[\phi_A, \mu_A, \mu_B])$, where the effective Hamiltonian is given by

subject to the initial condition $q(r, 0) = 1$ and suitable boundary conditions. The function $\mu(r, s)$ is a contour-related chemical potential field that depends on copolymer architecture. For example, in the case of diblock copolymers, it is given by:

$$\mu(r, s) = \begin{cases} \mu_A(r), & s \in [0, Nf] \\ \mu_B(r), & s \in [Nf, N] \end{cases} \quad (48)$$

Thermodynamic forces, i.e. first derivatives of H with respect to the three independent fields, must also be computed. These are given by

$$\frac{\delta H}{\delta \phi_A(r)} = \rho_0 \chi [1 - 2\phi_A(r)] - \rho_0 [\mu_A(r) - \mu_B(r)], \quad (49)$$

$$\frac{\delta H}{\delta \mu_A(r)} = \rho_0 \{ \tilde{\phi}_A(r, [\mu_A, \mu_B]) - \phi_A(r) \} \quad (50)$$

$$\frac{\delta H}{\delta \mu_B(r)} = \rho_0 \{ \tilde{\phi}_B(r, [\mu_A, \mu_B]) - [1 - \phi_A(r)] \} \quad (51)$$

The functionals $\tilde{\phi}_A$ and $\tilde{\phi}_B$ are “auxiliary volume fraction fields” and can be computed (for diblock copolymers) according to:

$$\tilde{\phi}_A(r, [\mu_A, \mu_B]) = \frac{1}{NQ} \int_0^{Nf} ds q(r, s) q^\dagger(r, N-s), \quad (52)$$

$$\tilde{\phi}_B(r, [\mu_A, \mu_B]) = \frac{1}{NQ} \int_{Nf}^N ds q(r, s) q^\dagger(r, N-s) \quad (53)$$

The propagator $q^\dagger(r, N-s)$ describes the statistical weight of a conjugate piece of copolymer and satisfies a slightly modified version of Eq (47).

● V.2 Dynamics

Models for the dynamics and rheology of inhomogeneous polymer melts can be constructed by embedding the above field theory into the formalism of irreversible thermodynamics. The “two-fluid model” is particularly convenient for this purpose. As discussed by Fredrickson (2002), it is possible to retain elastic stress and strain as dynamical variables in addition to the reduced density and chemical potential fields discussed above. Such a formulation would describe inhomogeneous, multiphase, viscoelastic flow. Ultimately, we hope to tackle such descriptions, but will begin by assuming that the elastic stress and strain variables are at local equilibrium, so that the viscoelastic stresses reduce to purely viscous stresses. This assumption is appropriate for flows that are slow on timescale of the stress relaxation time of the fluid. A second assumption is that the conjugate chemical potential fields, which reflect polymer degrees of freedom not contained

in the conserved order parameter ϕ_A , relax faster than ϕ_A and the conserved momentum density of the fluid.

With the above assumptions, the two-fluid model reduces to the following set of equations for the coupled fields:

$$\frac{\partial}{\partial t} \phi_A = -u \cdot \nabla \phi_A + \nabla \cdot \left[D(\phi_A) \nabla \frac{\delta H}{\delta \phi_A} \right] \quad (54)$$

$$\rho \frac{D}{Dt} u = \nabla \cdot \{ \eta(\phi_A) [\nabla u + (\nabla u)^T] \} - \phi_A \nabla \frac{\delta H}{\delta \phi_A} - \nabla P \quad (55)$$

$$\nabla \cdot u = 0 \quad (56)$$

$$\frac{\delta H}{\delta \mu_A} = \frac{\delta H}{\delta \mu_B} = 0 \quad (57)$$

In the above equations, ρ is the density, $u(r, t)$ is the velocity field of the medium, $D(\phi_A)$ is a diffusion coefficient, $\eta(\phi_A)$ is a shear viscosity coefficient, and $P(r, t)$ is a dynamic pressure field that is used as a Lagrange multiplier to enforce the incompressibility condition. The notation D/Dt denotes the usual convective derivative. Equations (18) can be viewed as equations of state that express μ_A and μ_B as explicit functionals of ϕ_A . These can be used to eliminate μ_A and μ_B expressing the thermodynamic force solely as a functional of ϕ_A .

This rich set of equations has not been employed before to study the coupled flow (u) and nanostructure (ϕ_A) of block copolymer melts subjected to shear and other types of flows. We believe that this is an excellent framework from which to launch numerical simulations of these phenomena.

● V.3 Results

The methodology outlined above has been applied to the study of phase diagrams for diblock copolymer systems, and the expected phase diagram is shown in *figure 24*,

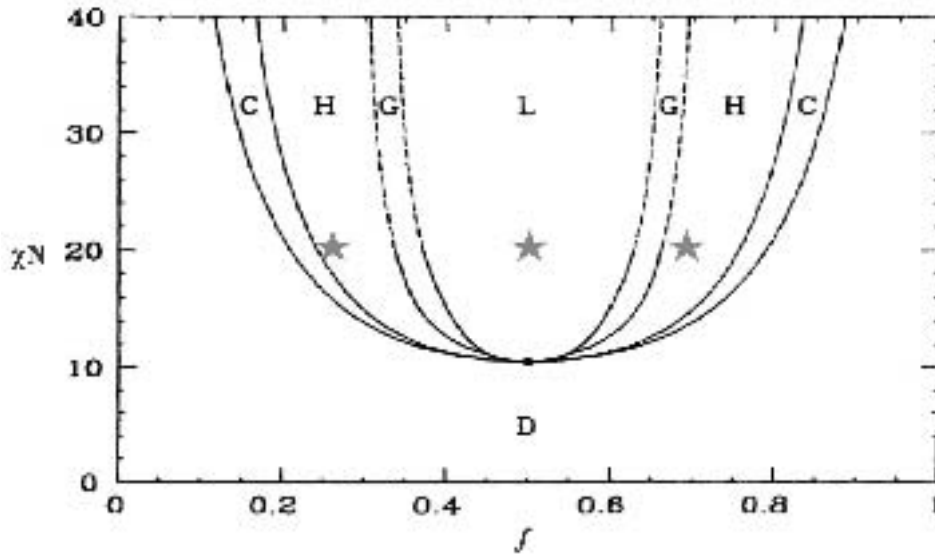
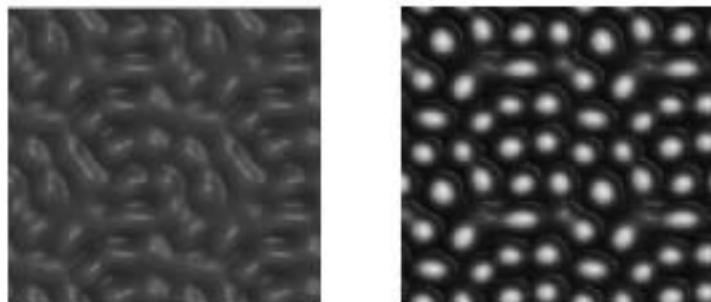
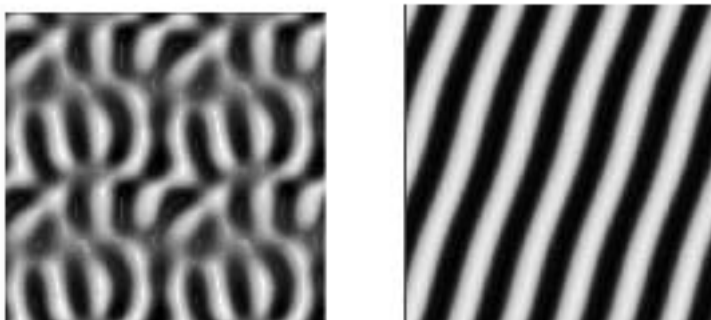


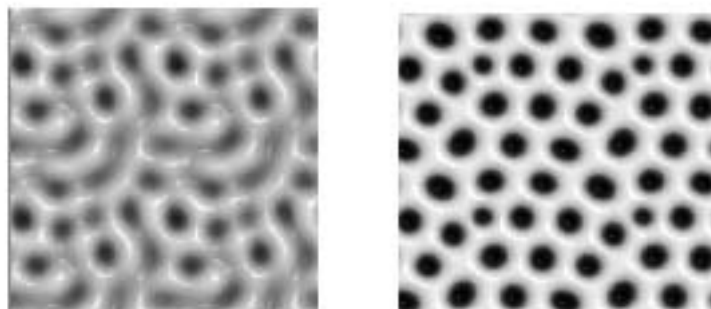
Figure 24: Phase diagram for a diblock polymer system. The ordinate is related to an inverse temperature and the abscissa is the concentration of one of the blocks. C stands for cylindrical structures, H for hexagonally-packed cylinders, G for gyroidal structures, and L for lamellae.



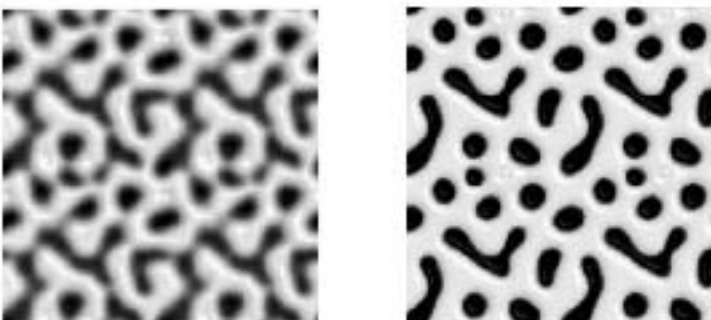
Row A: Hexagonally packed



Row B: Lamellae



Row C: Hexagonally packed



Row D: Gyroidal. The gyroidal state cannot be shown well in two dimensions.

Figure 25: FCFT calculations of equilibrium structure for the conditions in Figure 24, i.e., for a diblock system. The left column denotes an early time in the self-assembly process for the structures, and the right column close to the equilibrium state. Each row refers to a particular on the phase diagram.

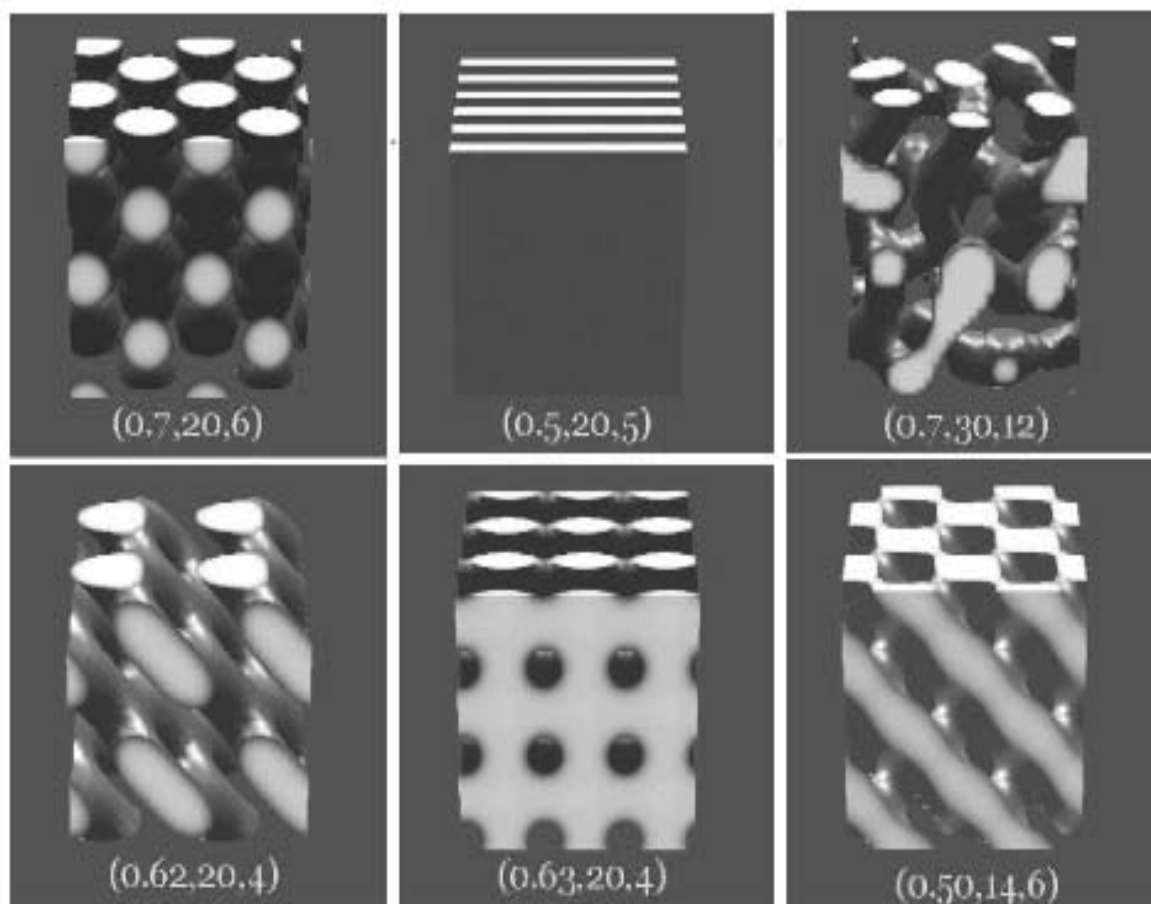


Figure 26: 3D calculations of diblock systems for various positions on the phase diagram. The numbers in parentheses in each panel denote: on the left-hand side, the polymer concentration; on the right-hand side, the inverse temperature. Note the complexity of the structures, which in this case are calculated assuming confinement and Neumann boundary conditions in the vertical direction.

Matsen and Schick (1996). The parameter in the ordinate is a sort of inverse temperature, and the abscissa is the concentration of AMB-block in the copolymer. C denotes cylindrical structures, H hexagonally-packed cylindrical structures, G gyroidal structures, and L lamellar structures. The SCFT calculations obtained in two dimensions for the regions shown by stars are given in *figure 25*. As can be seen, except for the gyroidal structures, which are not possible to display in two dimensions, the field theoretic calculations are accurate. In three dimensions, especially with confinement, more complex structures emerge, many of which are of interest to optical materials. These are shown in *figure 26*. Finally, we show the effect of shear on such structures as in *figure 27*, where it is clear that they are lamellar. An interesting aspect related to such lamellar structures is that they can go through a flipping, as illustra-

ted in *figure 28*, as an oscillatory shear rate is increased (see Koppi *et al.* (1992) and Hermel *et al.* (2002)). As these materials are of great interest as optical polymers, such flipping has profound implications. However, it is clear that to capture such behavior, the simple model, which is discussed here, has to be made more complex to include viscoelastic effects of the two-fluid type described earlier, and noise, which is associated with fluctuations near the order/disorder transition.

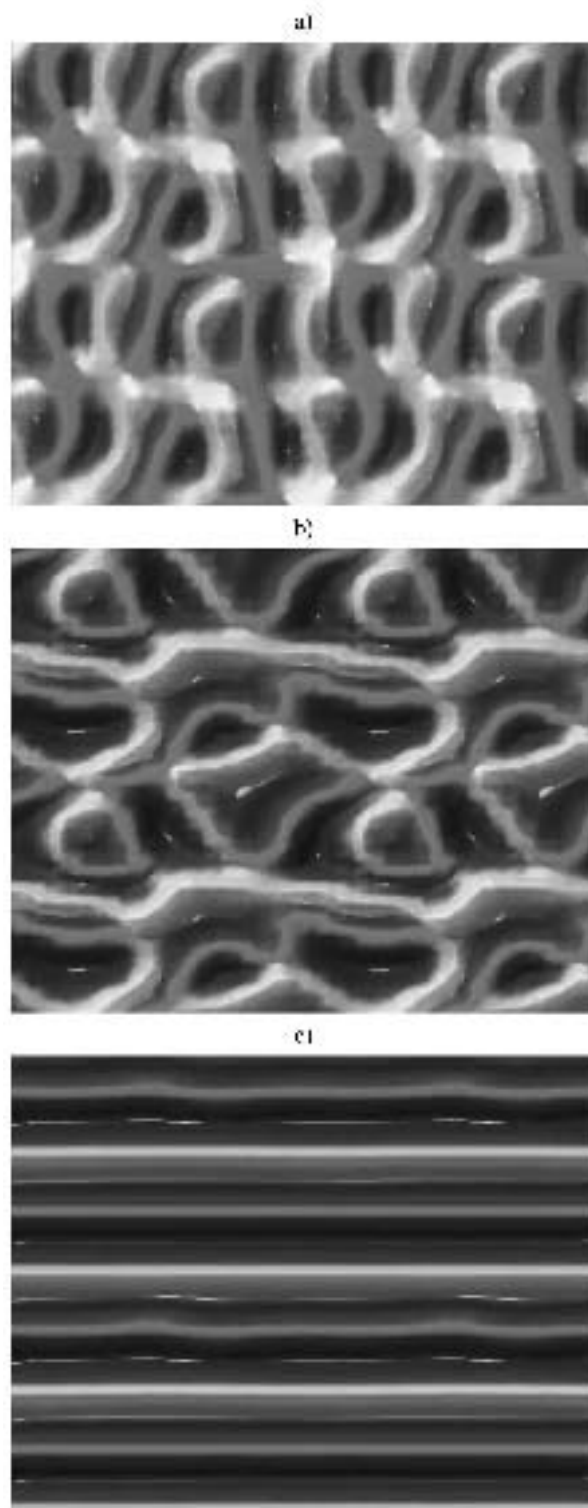


Figure 27: The effect of shear on a diblock system, shown at different times. Initially, the system wants to form a self-assembled cylindrical structure, but shear deforms these structures into lamellae. The panels are taken at different times, moving a) at an early time, to c) near equilibrium conditions under shear.

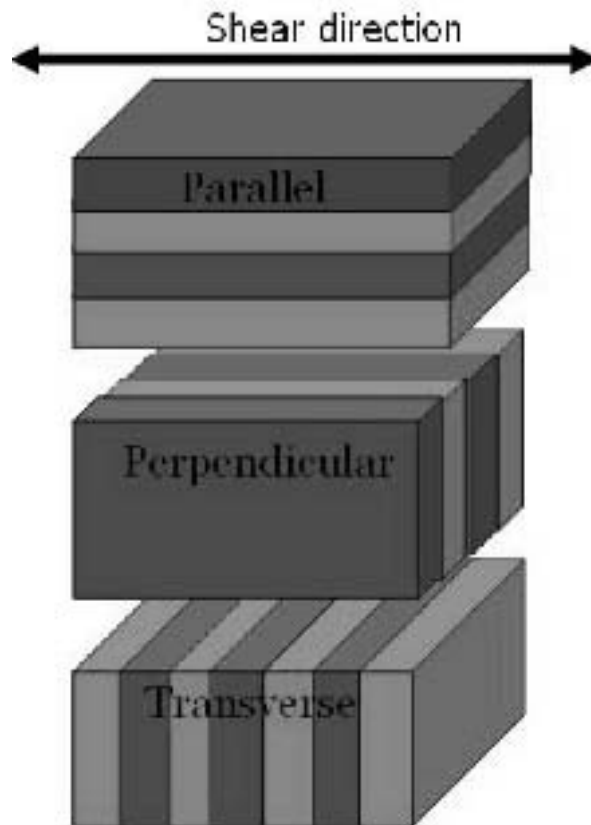


Figure 28: Flipping of lamellae structures in oscillating shear fields for diblock systems.

● V.4 Conclusions

In this paper we have outlined methods for directly resolving interfaces, first when they appear as contact discontinuities, which can be done using level-set and level-set/ghost fluid methods. The major problem with the methodology is to ensure conservation of mass (or volume) during events such as bubble mergers and break-ups. Progress has been made in this direction, and hybrid techniques such as particle/level-set combinations have been proposed, as well as variants on existing reinitialization procedures, such as suggested by Takahira *et al.* 2004. Level sets have been incorporated in commercial codes, and this methodology is therefore generally available for a variety of problems.

If one desires to resolve microscale structures, as they are important in many product formulations and multiphase materials such as homes, then phase-field/SCFT methods are of interest. Phase-field methods do not take molecular structure into account, and therefore they can be used to study phase separation in systems where universal classes of behavior emerge, i.e., simple fluids. For more complex molecules, such as multiblock polymers, the structures can self assemble into three-dimensional configurations that are defined by a minimum free energy. Such combined statistical mechanics/fluid mechanics models provide a framework that can capture structural features of many complex fluid formulations, and calculational methods are being intensely to solve such models. These are very rich free energy landscapes, and notable success has been obtained using the techni-

ques outlined here. The interest is for mesoscale structures, which cannot be easily resolved by molecular dynamics or Monte Carlo techniques, which nonetheless can be used to generate the free-energy landscapes, which are then used in the field theoretic framework. There is great interest in such methods, as structural features crucially affect desirable properties of many materials.

REFERENCES

- AXELSSON, O., 1977, "Solution of Linear Systems of Equations: Iterative Methods", Springer-Verlag, New York.
- BADALASSI, H.D., CENICEROS, H.D., and BANERJEE, S., 2003, "Computation of Multiphase Systems with Phase Field Models," *J. Comp. Phys.*, **190**, 371-397.
- BEUX, F. and BANERJEE, S. 1997, "Numerical Simulation of Three-Dimensional Two-Phase Flows by Means of a Level-Set Method," ECCOMAS 96 Proceedings, John Wiley. Bird, G. A., 1976 Molecular Gas Dynamics Clarendon Press, Oxford.
- BRACKBILL, J.U., KOTHE, D.B., and ZEMACH, C., 1991, "A Continuum Model for Modeling Surface Tension", *J. Comp. Phys.*, **100**, 335-354.
- BRAY, A.J., 1994, "Theory of Phase-Ordering Kinetics", *Adv. Physics*, **43**, 357-459.
- CANUTO, C., M.Y. HUSSAINI, A. QUARTERONI, T.A. ZANG, 1987, "Spectral Methods in Fluid Dynamics", Springer Verlag, New York.

- CHORIN, A.J., "Numerical Solution of the Navier-Stokes Equations", 1968, *Math. Comp.*, **22**, 745.
- DEANGELIS, V., P. LOMBARDI, P. ANDREUSSI, S. BANERJEE, 1999, "Microphysics of Scalar Transfer at Air-Water Interfaces", Proceedings of the IMA Conference: Wind-Over-Wave Coupling, Perspectives and Prospects, ed. Sajjadi, Hunt and Thomas, Oxford University Press.
- DEANGELIS, V., Ph.D. Thesis, Dept. of Chemical Engineering, UC Santa Barbara, 1998.
- EMMERT, R.E., PIGFORD, R.L., 1954, *Chem. Eng. Prog.* **50**, 87.
- FEDKIW, R. and LIU, Z.-D., 1998, "The Ghost Fluid Method for Viscous Flows", *Progress in Numerical Solutions of Partial Differential Equations*, Arachon, France, edited by M. Hafez.
- FEDKIW, R., *et al.*, 1999, "A Non-Oscillatory Eulerian Approach to Interfaces in Multimaterial Flows (The Ghost Fluid Method)", *J. Comput. Phys.*, **152**, 457-492.
- FREDERICKSON, G.H., 2002, "Dynamics and Rheology of Inhomogeneous Polymeric Fluids: A Complex Langevin Approach," *J. Chem. Physics*, **117**.
- FREDRICKSON, G.H., GANESAN, V., and DROLET, F., 2002, "Field-Theoretic Computer Simulation Methods for Polymers and Complex Fluids," *Macromolecules* **35**, 16-39.
- GANESAN, V., and FREDRICKSON, G.H., 2001. "Field-Theoretic Polymer Simulations," *Europhys. Lett.* **55**, 814.
- HARLOW, F.H., WELCH, J.E., 1965, "Numerical Calculation of Time-Dependent Viscous Incompressible Flow of Fluid with a Free Surface", *Phys. Fluids*, **8**, 2182-2189.
- HASHIMOTO, T., MATSUZAKE, K., MOSES, E., ONUKI, A., 1995, "String phase in phase separating fluids under shear flow," *Phys. Rev. Letters*, **74**, 126.
- HERMEL, T.J., LIFENG WU., HAHN, S.F., LODGE, T.P. and BATES, F.S., 2002, "Shear-Induced Lamellae Alignment in Matched Triblock and Pentablock Copolymers," *Macromolecules* **35**, 4685.
- HIRT, C.W., NICHOLS, B.D., 1981, "Volume of Fluid (VOF) Methods for the Dynamics of Free Boundaries", *J. Comp. Phys.*, **39**, 201-25.
- KANG, M., FEDKIW, R., LIU, X.-D., 1999, "A Boundary Condition Capturing Method for Multiphase Incompressible Flow", CAM Report 035.
- KOPPI, K.A., TIRRELL, M., and BATES, F.S., 1992. "Orientational Transitions in Block Copolymers Under Shear," *J. Phys. II*, **2**, 1941.
- LANGER, J.S., 1992, "Solids Far From Equilibrium", edited by C. Godreche, p. 297, Cambridge University Press.
- LAUFAURIE, B., NARDONE, C., SCARDOVELLI, R., ZALESKI, S., ZANETTI, G. 1994, "Modelling Merging and Fragmentation in Multiphase Flows with SURFER," *J Comput. Phys.* **113**, 134-147.
- LIU, X.D., OSHER, S. and CHAN, 1994, "Weighted Essentially Non-Oscillatory Schemes", *J. Comp. Phys.*, **115**, 200-212.
- LIU, X.D., FEDKIW, R.P. and KANG, M., "A Boundary Condition Capturing Method for Poisson's Equation on Irregular Domains", *J. Comp. Phys.*
- LOMBARDI, P., DEANGELIS, V., and S. BANERJEE, 1996, "Direct Numerical Simulation of Near-Interface Turbulence in Coupled Gas-Liquid Flow," *Phys. Fluids* **8**, 1643.
- MATSEN, W.W., and SCHICK, M., 1996, "Self-Assembly of Block Copolymers," *Curr. Opin. Colloid Interface Sci.* **1**, 329.
- MISAWA, M., *et al.*, 1996, "Bubble Detachment and Flow Pattern Change in Shear Flow under Microgravity Conditions", *Proc. INSPACE '96*, Tokyo, 543-560.
- MISAWA, M., *et al.*, 1997, "Bubble Growth and Detachment in Shear Flow under Microgravity Conditions", *Experimental Heat Transfer, Fluid Mechanics and Thermodynamics*, 1997, ed. Giot M., *et al.* 987-994.
- NAVE, J.C., BANERJEE, S., 2004, "Direct Numerical Simulation of Wavy Falling Liquid Films", *Proc. 5th Int. Conf. on Multiphase Flow*, ICMF '04, Yokohama, 423.
- NAVE, J.C., 2004, "Direct Numerical Simulation of Liquid Films", Doctoral Dissertation, Department of Mechanical Engineering, University of California, Santa Barbara, September 2004.
- NOSOKO, T., and P.N. YOSHIMURA, 1996, "Characteristics of Two-Dimensional Waves on a Falling Liquid Film", *Chem. Eng. Sci.*, **51**, 725.
- OSHER, S., SETHIAN, J., 1988 "Fronts Propagating with Curvature-Dependent Speed: Algorithms Based on Hamilton-Jacobi Formulations", *J. Comput. Phys.* **79**, 12-49.
- PRESS, H.W., TEUKOLSKY, S.A., VETTERLING, W.T., FLANNERY, B.P., 1992, "Numerical Recipes in C", 2nd Ed., Cambridge University Press.
- SHU, C.W., and OSHER, S., 1988, "Efficient Implementation of Essentially Non-Oscillatory Shock Capturing Schemes", *J. Comp. Phys.*, **88**, 439-471.
- SUSSMAN, M., SMEREKA, P., OSHER, S. 1994 "A Level-Set Approach for Computing Solutions to Incompressible Two-Phase Flow," *J. Comput. Phys.* **114**, 146-159.
- SUSSMAN, M., and SMEREKA, P., 1997, "Axisymmetric Free Boundary Problems", *J. Fluid Mech.* **341**, 269-294.
- SUSSMAN, M., *et al.*, 1998, "An Improved Level-Set Method for Incompressible Two-Phase Flows", *Comput. Fluids*, **27**, 663-680.
- SUSSMAN, M., *et al.*, 1999, "An Adaptive Level-Set Approach for Incompressible Two-Phase Flows", *J. Comp. Phys.*, **148**, 81-124.
- TAKAHIRA, H., HORIUCHI, H., and BANERJEE, S., 2004, "An Improved Three-Dimensional Level-Set Method for Gas-Liquid Two-Phase Flows", *J. Fluids Engr (ASME)* **126**, 578-585.
- UNVERDI, S., TRYGGVASON, A., 1992 "A Front-Tracking Method for Viscous, Incompressible Multi-Fluid Flows", *J. Comput. Phys.* **100**, 25-37.
- VAN DER VORST, H.A., 1992, "Bi-CGSTAB: a Fast and Smoothly Converging Variant of Bi-CG for the Solution of Nonsymmetric Linear Systems", *SIAM J. Sci. Stat. Comput.* **13**, 631-644.
- ZANG, Y., *et al.*, 1994, "A Non-Staggered Grid, Fractional Step Method for Time-Dependent Incompressible Navier-Stokes Equations in Curvilinear Coordinates", *J. Comp. Phys.*, **114**, 18-33.
- ZANG, Y., and STREET, R.L., 1995, "A Composite Multigrid Method for Calculating Unsteady Incompressible Flows in Geometrically Complex Domains", *Int. J. Numer. Methods in Fluids*, **20**, 341-361.